Renewable and Sustainable Energy Reviews 137 (2021) 110361

Contents lists available at ScienceDirect

Renewable and Sustainable Energy Reviews

journal homepage: http://www.elsevier.com/locate/rser

State of the art in composition, fabrication, characterization, and modeling methods of cement-based thermoelectric materials for low-temperature applications

Xiaoli Liu [a], Ruchita Jani [b], Esther Orisakwe [c], Conrad Johnston [c], Piotr Chudzinski [c], Ming Qu [a,*], Brian Norton [b], Niall Holmes [b], Jorge Kohanoff [c], Lorenzo Stella [c,d], Hongxi Yin [e], Kazuaki Yazawa [f]

[a] Lyles School of Civil Engineering, Purdue University, West Lafayette, IN, USA
[b] School of Civil and Structural Engineering, Technological University Dublin, Ireland
[c] School of Mathematics and Physics, Queen's University Belfast, United Kingdom
[d] School of Chemistry and Chemical Engineering, Queen's University Belfast, United Kingdom
[e] International Center for Energy, Environment & Sustainability, Washington University in St Louis, St Louis, MO, USA
[f] Birck Nanotechnology Center, Purdue Univeristy, West Lafayette, IN, USA

ARTICLE INFO

Keywords:
Thermoelectric cement composites
Additives
Thermoelectric generator
Thermoelectric cooler
Seebeck coefficient
Figure of merit

ABSTRACT

The worldwide energy crisis and environmental deterioration are probably humanity's greatest challenges. Thermoelectricity, which allows for the mutual conversion between thermal and electrical energy, has become a promising technology to alleviate this challenge. Increasingly more research focuses on how to fabricate and apply thermoelectric materials for harvesting energy and regulating the indoor thermal environment. However, only a few studies have focused on cementitious materials with thermoelectric potential. Thermoelectric cement is a composite material in which particular additives can enhance the thermoelectric performance of ordinary cement. By potentially replacing traditional construction materials with thermoelectric cement in building applications, electricity could be generated from waste heat, reducing the use of fossil fuels, and supplementing other renewable energy sources like solar and wind. This article presents a review of fundamentals, fabrication, characterization, composition, and performance, as well as modeling methods and opportunities for thermoelectric cement composites. The literature reviewed covers the period from 1998 to 2020 related to thermoelectric cement. It also presents the challenges and problems to overcome for further development and provide future research directions of thermoelectric cement.

1. Introduction

The energy needs of the planet have increased substantially over the last few decades. In 2018, world energy consumption increased by 2.3% compared to the previous year (about 590 Quadrillion BTUs of primary energy in 2017), double the average increase since 2010 [1]. About 80% of the global energy is provided by combusting fossil fuels [1,2], a resource that, being non-renewable, keeps depleting with continuous usage. Moreover, the exhausted gases and other emissions from the combustion can contribute to the greenhouse effect, thus resulting in global warming with its detrimental impact on the environment. To alleviate the dual crisis of energy and environment, while maintaining economic growth, people are seeking sustainable energy generation and energy-efficient technologies [3,4].

Using thermoelectric (TE) materials to harvest waste energy is one of the promising technologies to address the challenge. TE materials can work as a generator (TEG) to generate electrical potential due to a temperature gradient through a phenomenon named the Seebeck effect [5]. The power generation capability of the TEG is given via the Seebeck coefficient $S = -\Delta V/\Delta T$, i.e. the voltage generated due to a temperature difference [6]. The TEG has been generally used for power generation through harvesting waste heat in automobiles [7,8], power plants [9], even in space applications [10–12]. The TE material can also work in the opposite way according to the Peltier effect [13], in which the

* Corresponding author.
E-mail address: mqu@purdue.edu (M. Qu).

https://doi.org/10.1016/j.rser.2020.110361
Received 12 March 2020; Received in revised form 22 August 2020; Accepted 7 September 2020
Available online 12 November 2020

power input will lead to a temperature difference between the two extremes of the TE material. Hence, the TE material is used as a thermoelectric cooler/heat pump (TEC/TEH). TEC/TEH applications include electronic devices [14], refrigeration systems in vehicles [15], and wearable cooling systems [16]. The overall performance of a TE material is measured by the figure of merit, $ZT = S^2\sigma T/\kappa$, which is determined by the operating temperature T and three intrinsic TE properties such as the Seebeck coefficient (S), electrical conductivity (σ), and thermal conductivity (κ). (See fundamentals of TE phenomenon in Appendix).

Recently, there has been an increased interest in using the potential of the TE technology within buildings. Previous research incorporated commercially available TEGs into pavements for both generating power and cooling the road surface [17–21]. TEC/TEH has also been applied to the building envelope for actively cooling or heating the building by using the electricity from the photovoltaic system. Other existing studies used alloy-based TEMs into walls [22–27] and roofs [28,29], demonstrating TEC/TEH's ability to adjust the room temperature and reduce the load on air conditioning systems. Additionally, cement-based TEG or TEC/H systems, which integrate into the existing building envelope, is another alternative for harvesting ambient energy based on TE [30]. Previous reviews in the field of thermoelectricity have focused on materials [31–39], fabrication [34,40,41], characterization [42], designs [43] and applications [8,32,35,44–53] of TE materials. However, there is few review on TE cement, which is quite different from these conventional TE materials at the aspects. Also, the modeling methods used in traditional TE materials for the performance analysis and design optimization could not apply to TE cement composites. Hence, there is a need for a review to address the latest progress and challenges in the development of an effective commercially viable TE cement. In this paper, we first review the fabrication methods for developing TE cement composites in Section 2. The strengths and drawbacks, and challenges of the existing methods employed to characterize the TE properties of cement composites are summarized and compared in Section 3. Section 4 is about the recently emerged TE cement composites and their TE properties. Section 5 is the review of the modeling methods for both TE materials and TE cement composites. The last section, Section 6, concludes the review and gives challenges and future research directions.

1.1. Materials and methodology

Scopus and Google Scholar databases are the primary resources of the articles included in the review. The cement-based TE materials are related to multiple disciplines, and some of them are interdisciplinary. Scopus, Google Scholar, and Web of Science are currently the most used databases for researchers. Compared to Web of Science, Scopus and Google Scholar cover more interdisciplinary studies from a broader range of publications published both inside and outside North America. Web of Science contains papers in a more extended period, but a relatively smaller number of journals, only about 62% of the journals that Scopus has. Besides, the cement-based TE materials is a recently emerged research field. Scopus, thus, is a better database because it includes in-press articles, which are the most recent publications. The first part of the paper presents a comprehensive review of the experimental studies, including fabrication (Section 2), characterization (Section 3), and performance analysis (Section 4) for TE cement composites. The literature comes from papers listed in Scopus that contain the keywords "thermoelectric" (or "Seebeck") and "cement" in titles and abstracts. The articles were filtered by removing ones unrelated to TE cement. The final result obtained on 07/28/2020 revealed that there were 56 relevant items, covering the research period from 1998 to 2020. In some interest areas of this review, there are many articles specifically addressing composite cement, while in other areas, the material is limited. Additionally, articles concerning ordinary cement were considered (i.e., research methods characterizing thermal conductivity or electrical conductivity for ordinary cement). Section 5 presents modeling opportunities for TE cement composites. In Section 5.1-5.3, keywords such as "cement" and "atomistic" were used to find initial articles, as well as keywords related to specific techniques and methods (e.g., "Density Functional Theory," "Force field," "Boltzmann Transport"). There was very little material related explicitly to TE cement, and so to increase the usefulness of this review article, the atomistic modeling efforts related to ordinary cement are highlighted, and the relevant techniques outlined for the benefit of the widest possible readership. In Sections 5.4-5.6, describing macroscopic models, materials were found by searching for references containing "thermoelectric" and "module" and "model" in titles and abstracts, returning several hundred articles in the period from 2015 to 2020. The articles were first scanned and classified into the device-level and system-level modeling, and the latter were discarded. While many models have been proposed at the device level, they share ideas (i.e., using a simple model or commercial simulation software). So, in this article, general techniques or ideas are summarized for the broadest audience and only selected vital articles focusing on the model development for TE modules are highlighted.

2. Fabrication methods of TE cement composites

The application of TE technology in buildings attracted academia's attention in recent years. Researchers developed the TE building envelope to realize either power generation (e.g., when applying temperature difference between indoors and outdoors) or room temperature regulation (e.g., when electricity is applied). The TE building envelope may use either commercially available thermoelectric modules (TEMs) or newly developed TE materials. When applied the commercial TEM into the simplified building envelope made of thin insulation, the TEM had an aluminum panel and thick heat sinks to dissipate heat. However, in real applications, the building envelope is made of different layers of insulation, board, and, most importantly, the concrete/brick, which has low thermal conductivity. The newly developed TE materials are cementitious-based. Researchers have found that adding specific materials to the cement can improve the structural strength of concrete as well as introducing TE properties. The TE building envelope with TE cement requires less system complexity and better integrality. The following sections 2 to 4 review the TE enhanced cement composites at low operating temperatures (under 100 °C) reported in the literature from 1998 to 2020, at three significant aspects of fabrication, characterization, and performance analysis. This section described the fabrication methods for the TE cement composite. The type and amount of materials used in the manufacture of different TE cement composites in the published literature are summarized in Table 2.

2.1. The wet method

There are two different fabrication methods for TE cement composites used in the lab: the conventional wet mixing and dry mixing/compression. The standards for manufacturing concrete specimen using the wet mixing method can be found in ASTM C192/C192 M [54] and C31/C31 M [55]. Those procedures are revised for TE cement composites by dispersing and introducing additive materials into the cement powder first. The following bullets summarize the four processes of making TE cement composites, including dispersing, mixing, molding, and curing.

(1) Dispersant and additives (e.g., carbon fiber, metal powder) are first added to water. Then the defoamer is added into this wet mixture. The wet mixture of additives can be further treated by ultrasonic wave to obtain the even distribution of fibers/powders in the solution.
(2) The wet additive mixture, cement powder, acid super-plasticizer (water reducer), and silica fume (if applicable) are mixed.

(3) The final wet mixture is poured into the mold to generate the sample with a designed geometry. Then a vibrator is used to reduce bubbles inside the sample and form smooth surfaces. The specimen needs to stay in the mold for 24 h to obtain hardened cement paste.
(4) After 24-h molding, the cement specimen can be de-molded and put into a temperature and humidity-controlled chamber for curing. TE cement specimen is usually cured for 3–21 days at room temperature and relative humidity of 95%.

2.2. The dry method

The dry mixing and compression method was used to make TE-enhanced cement composites by Wei et al. [56–58] and other researchers [59,60]. In the dry method, the cement powder and additives were mixed without the use of water reducer and dispersant (e.g., cellulose) so that the electrical conductivity can be improved. Besides, due to the high-pressure treatment, the porosity of the sample becomes lower. It provides a dense structure and excellent TE performance for the cement composite. The following bullets summarize the necessary procedures for making TE cement specimens using the dry method (Fig. 1).

(1) Use a mill ball to grind cement to reduce the size of particles.
(2) Weigh all raw materials and mix them. Pour the dry mixture into the grinding wheel type sand mixer and get it evenly mixed by observing the color becomes uniform grey.
(3) Pour an appropriate amount of homogeneous mixture into the customized cylindrical stainless-steel mold with a metal strip and die block. A mechanical system will apply the pressure at 40–60 MPa to the metal strip, which compressed the dry mixture into a compact cylinder.
(4) Put the compact sample on a sponge saturated by water to absorb water through the capillarity effect. Then the sample will be exposed to the humid environment with relative humidity above 95% for pre-curing.
(5) In the final curing, soak TE cement samples in a tank full of water for three days at room temperature.

2.3. Discussions, challenges, and future research directions in sample fabrication

As the procedures of both wet and dry methods are described in detail, the strength and drawbacks of the two methods, the suggestions for sample fabrication, and suggested future research directions are presented as follows.

- The wet method is easy to operate, and the sample yield is higher. But the dispersion of additives is essential and challenging. The effective dispersing agent and the ultrasonic or magnetic device for mixing are usually required to ensure that the additive can be evenly distributed in the solution and cement matrix. This wet mixing procedure can bring air bubbles into the cement matrix and generate pores in the sample, which reduces the effective contact of additives and results in lower thermal and electrical conductivity value.
- The dry method avoids the use of chemical dispersants, defoaming agents, and water-reducing agents, thus significantly increasing the electrical conductivity of the sample. But this method requires a device to provide high pressure and the pressure-resistant mold. The amount of dry mixture poured in the mold need to be controlled accurately to ensure the identical size of samples, and thus. Samples made by the dry method have low porosity and high density, but if not correctly handled, they may encounter internal cracks to degrade the TE performance.
- After the curing in both dry and wet methods, some researchers dry the sample entirely in the oven to remove free water inside the sample. However, this step might cause cracks to the sample due to the intense thermal stress. Besides, the water content in the cement is hard to control because cement will absorb/release vapor from/to the ambient environment to achieve a balance of surface vapor pressure. For stable characterizations, it is recommended to store samples in a humidity-controlled environment close to the testing environment, until the internal structure of the specimen tends to be stable.
- Many TE cement composites are made by either the wet method or the dry method. Although the cement composite employed the latter method exhibited higher TE performance, there is still no direct and substantial comparison of the TE properties of the samples made in two different ways. Which method can improve the TE performance of cement composite is still an interesting research question. Besides, the study on the mechanical properties of the samples made by two different methods is also crucial to determine whether TE cement can be used as a load-bearing component.

3. Characterization methods of TE cement composites

Thermoelectric material development needs to measure physical parameters such as the Seebeck coefficient, electrical conductivity, and thermal conductivity accurately. These parameters combined can provide insights about the potential figure of merit (*ZT*) of a TE material, which can further help in determining its efficiency and quantifying the power generation. This section investigates the most commonly adopted

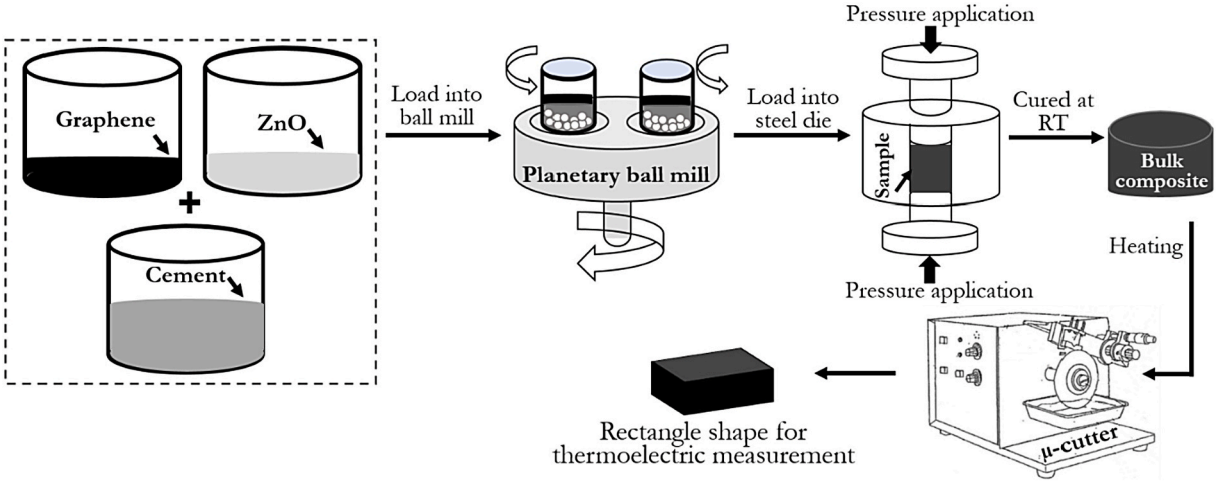

Fig. 1. Processes of sample preparation using the dry method (Figure was obtained from Ref. [60]).

methods in literature to measure the three TE properties mentioned above for cementitious materials.

3.1. Electrical resistivity measurement

Electrical resistivity (ρ) indicates the ability of a material to resist the flow of electric current, which is the inverse of electrical conductivity (σ) [61]. The electrical resistivity of a material is generally obtained by measuring its electrical resistance relative to its geometry [62].

3.1.1. The uniaxial method or bulk electrical resistance testing

The uniaxial method consists of two electrodes in the form of metal plates placed at both the ends of a sample along with a moist sponge in between to ensure appropriate electrical contact, as shown in Fig. 2a. An alternating current is applied to the electrode, and the ratio of drop voltage generated due to the current is measured as resistance. This method is more suitable for making laboratory-based measurements [62].

3.1.2. Four-probe method for resistance testing

The Wenner probe or four-probe method (Fig. 2b) employs four electrodes to measure the sample resistance. The two inner electrodes are used for potential measurements while the two outer electrodes are used for supplying current. The main difference between the uniaxial and the four-probe method is that for the latter, current and voltage measurements are carried out at separate electrodes so that the impact of interfacial resistance could be eradicated, providing better accuracy of measurements. This method measures resistivity values from the surface of the sample; hence it can be used for on-site measurements for any shape of the sample.

3.1.3. Surface disc method for resistivity testing

The surface disc method uses an electrode in the form of a disc arranged on top of the sample under test consisting of rebar to determine its resistivity (Fig. 3). The steel rebar is required to have continuity throughout the sample and possess a connection to the reinforcement cage. A cell constant obtained by dividing the gap between the two measurement points, along with its cross-sectional area, is required for obtaining the resistivity value from the measured resistances. It is challenging to get precise measurements of cell constant as it depends on the cover depth. It is thus obtained either empirically using concrete samples with known resistivity values or taken as 0.1 m for a cover depth, with bar and disc diameters between 10 and 50 mm [63]. The resistivity of the sample can be evaluated using Eq (3.1). The limitation of this method is that it can only be used for samples consisting of embedded rebar.

$$\rho = 0.1 \times R(disc - rebar) \tag{3.1}$$

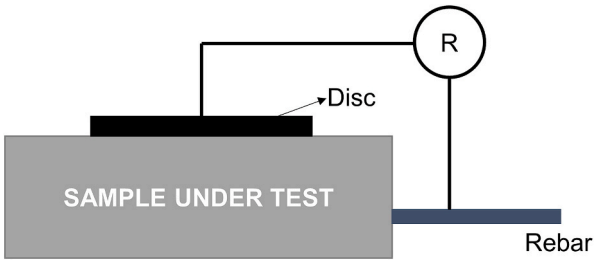

Fig. 3. Surface Disc method for electrical resistivity measurement (reproduced from Ref. [63]).

Another method used for resistivity measurements is the square array probe, which works using a similar principle as the four-probe method. Electrodes are arranged in a square array where two electrodes act as current injectors, and the opposite two electrodes measure the voltage difference. The spacing between the electrodes is kept somewhere between 50 and 100 mm [64].

3.2. Thermal conductivity measurements

Thermal conductivity (k) of a material can be established as the amount of heat transferred by a material of unit thickness in a direction perpendicular to its unit surface area when subjected to a unit temperature gradient [65,66], as expressed by Fourier's law [67]. It is essential to study the thermal characteristics of building materials like cement and concrete as they help determine the energy consumption in buildings [68]. Thermal conductivity can be measured using two methods, steady-state and transient [69,70], as presented below. The steady-state method takes a longer time [71,72] but gives more accurate results. The transient method is used in a system where the temperature is varying with time, which reduces measurement time and gives quicker results. It is more suitable for samples having a non-uniform composition of heterogeneous materials and also for materials that contain moisture, which includes cement mortar and concrete [71,72].

3.2.1. Box method (steady-state)

The set up for the box method [73] comprises of cold and hot chambers where the sample is fixed such that no lateral heat flow exists, as shown in Fig. 4a. When the specimen is subjected to cold temperatures on one side and hot on another, it leads to a heat flow being established [73]. Once a steady-state unidimensional heat flow is achieved, by measuring the temperature difference on both sides of the sample, by considering the amount of heat flowing from the hot to the cold, the thermal conductivity can be calculated using Eq. (3.2) where Q is the heat flux.

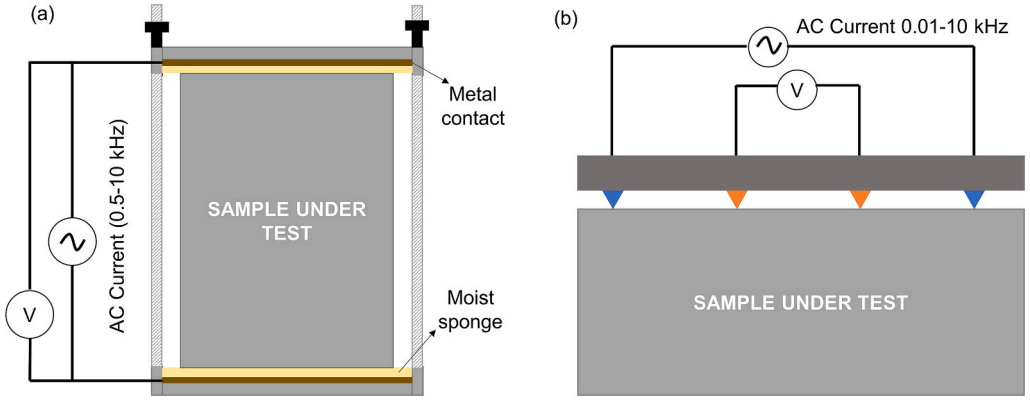

Fig. 2. (a) Uniaxial method and (b) four-probe method for electrical resistivity measurement (reproduced from Ref. [62]).

$$k = \frac{Q\ x}{A.\Delta T} \tag{3.2}$$

3.2.2. Guarded hot plate method (steady-state)

The guarded hot plate (Fig. 4b) is another steady-state technique for thermal conductivity measurements where the tested sample is placed between hot and cold plates. The system is well insulated from all sides. Depending upon the size and the number of hot and cold plates in the setup, more than one sample can be tested at a time. The sample is exposed to unidirectional heat flow from the hot to the cold side due to the temperature difference, which becomes constant once a steady state is achieved by the system. The temperature difference that exists between two sides of the sample and the amount of heat flow as a result of it leads to the thermal conductivity values using Eq. (3.2) [74].

3.2.3. Hot-wire method (transient)

The transient hot-wire method (Fig. 5a) works on the principle of evaluating the rise in temperature with respect to time of a linear heat source (wire) which is inserted in the middle of the sample [75]. The hot wire/probe is used as a heat source and can be regarded as an infinite source of heat. The ratio of its length to radius should be higher than 200 [75]. The wire also has an embedded temperature measuring sensor [76]. Upon inserting the wire into the sample, a constant heat flux (q) along the length of the wire is supplied, and the increase in temperature (dT) [77] with respect to time is recorded by the system. The thermal conductivity of the material can be derived using Eq. (3.3):

$$k = \left(\frac{q}{4\pi}\right)\left(\frac{dT}{d(\ln t)}\right)^{-1} \tag{3.3}$$

3.2.4. Transient plane source method

The transient plane source method (Fig. 5b) involves the use of a thin disc that supplies heat, which is a temperature-dependent resistor for thermal conductivity measurements and also acts as a temperature-sensing device [78]. This technique was introduced by Gustafsson [79] for measuring the thermal conductivity of smaller sized samples. In this method, a thin sensor is sandwiched between two halves of the specimen being tested. A direct current is applied to the disc to increase the temperature of the disc by 1–2 K [78]. Due to the rise in temperature, the electrical resistance of the sensor changes. This will cause a change in the voltage across the resistor, and the change in voltage and current across and through the resistor over time can be measured. By comparing this with the supplied current provided initially for heating the sensor, the amount of heat flow taking place between the sample and disc sensor can be calculated [78,79]. The thermal conductivity (k) can be obtained by considering the average rise in the temperature of the sensor ($\Delta\overline{T}(\tau)$) with respect to time using Eq. (3.4), where P_o represents the heat supplied from the sensor, r is the radius of the disc sensor, and τ is a parameter which can be derived from the thermal diffusivity [78,79] and can also be derived from the values of change in resistance.

$$\Delta\overline{T}(\tau) = \frac{P_o}{\pi^{3/2} rk} D(\tau) \tag{3.4}$$

3.2.5. Laser flash diffusivity method

The laser flash method (Fig. 6) is another transient way to determine the thermal conductivity of a material indirectly. This method is used to obtain the thermal diffusivity of a sample, which is usually required to be a small coin-sized cylinder. It was first introduced by Parker in 1961 [81]. In this technique, the sample is subjected to a short-pulsed laser from the front end, and the change in temperature as a result of it in the rear side of the sample is measured using an infrared detector. The half time (i.e., the time required for the signal to reach its half-height) is noted, and using the sample thickness, the thermal diffusivity can be evaluated. It is necessary to know the specific heat capacity of the sample to find the therm al conductivity by using the diffusivity measured [82]. The advantage of this method is that it does not require any heat flow within the sample or a temperature gradient established for measurements. Even at high ranges of temperature, the variability in the measured values is within a span of 3–5%, making it a very reliable method for deriving thermal conductivity [83–85]. The disadvantage is that an additional differential scanning calorimeter (DSC) is required for finding the specific heat capacity of samples, and the apparatus is highly sophisticated.

3.3. Seebeck coefficient measurement

The Seebeck coefficient can be obtained by measuring the electric potential under a given temperature difference at two extremes of a material. In the most simplified Seebeck measurement system for the cement specimen, the hot-side temperature of the sample is controlled by the electrical heater, and the cold side is exposed to the ambient without temperature control [58,86–96]. Thermocouples for temperature measurement are placed at two ends of the sample, and the electrodes for potential measurement are placed on the same surfaces. The configuration is shown in Fig. 7a. This set up can also be used to measure the two-probe electrical conductivity alternately. However, for samples with low electrical resistivity, a four-probe arrangement is preferred to measure the two-probe Seebeck coefficient along with the four-probe electrical conductivity [56,57,97], as shown in Fig. 7b. This

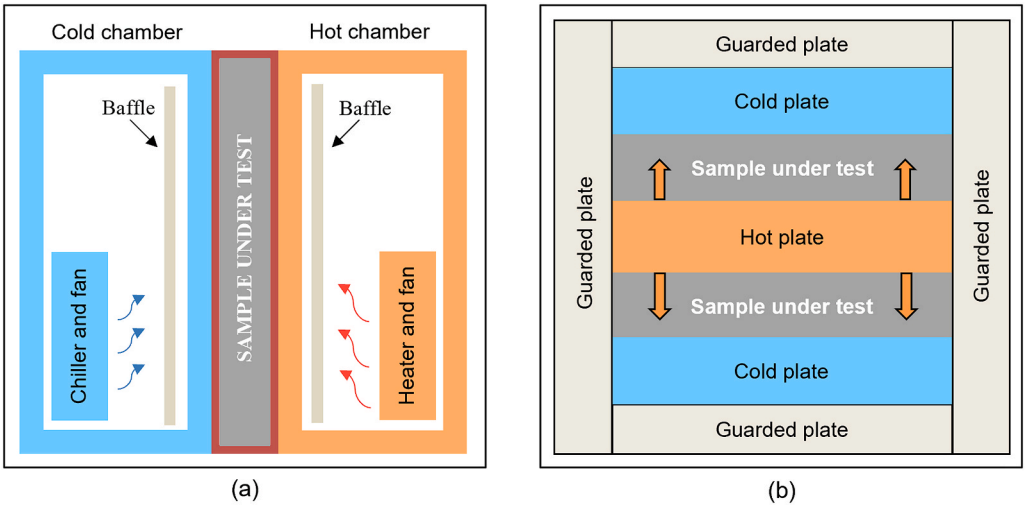

Fig. 4. (a) Steady-state hot box method and (b) guarded hot plate method for thermal conductivity measurement.

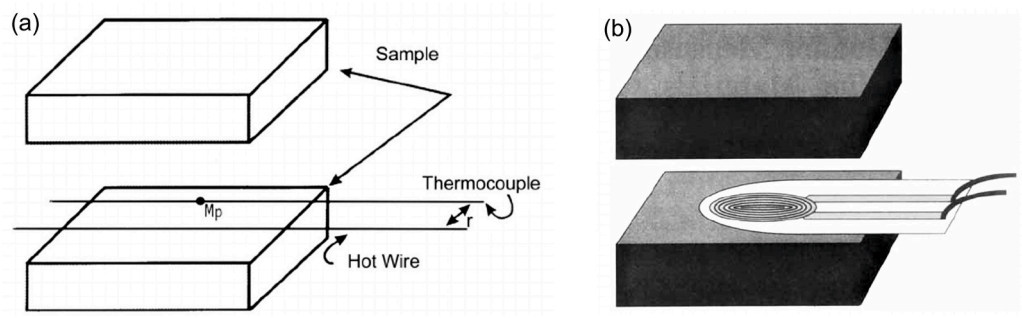

Fig. 5. (a) Transient Hotwire (sourced from Ref. [80]) and (b) plane source method for thermal conductivity measurement (sourced from Ref. [78]).

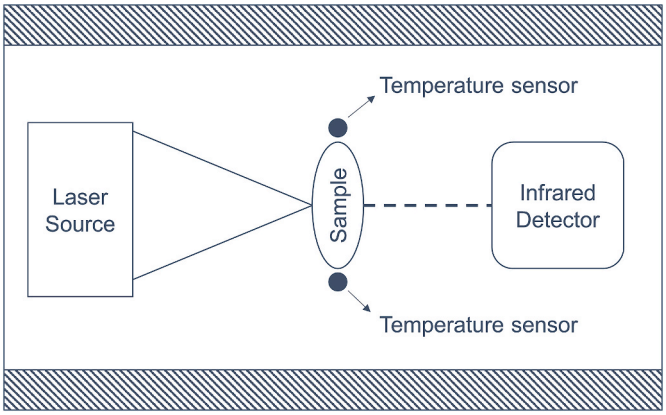

Fig. 6. Laser Flash Diffusivity method for thermal conductivity measurement.

arrangement provides improved thermal and electrical contact by eliminating contact resistance. Besides, there also has a four-probe Seebeck measurement, including both temperature and potential characterizations at four points along with the sample, to obtain the non-linear V-T curve. Other than the customized setup, Ghosh et al. employed a more advanced device, such as RZ2001i Ozawa Science equipment [59,60], to directly measure the Seebeck coefficient for cement composites. Besides, many other commercially available equipment can be used to characterize the TE cement composite, for instance, the DynaCool™ Physical Property Measurement System (PPMS) [98]. The advantages of these advanced devices are excellent thermal insulation, reduction of interference from external electromagnetic fields, precise temperature control, high reliability, etc. But the adaptability of the device for cement composites depends on many aspects, such as limitations for sample size, operating conditions, Seebeck signals (must be suitable for selected amplifier and voltmeter), etc. Generally, the measurement of Seebeck coefficient requires three points of attention: ensuring that temperature and potential are measured from same surfaces, ability to capture low electrical signals reliably, and good thermal and electrical contacts. Table 1 presents a summary of different methods that have been used in literature to characterize the TE properties of cement-based TE materials.

3.4. Discussions, challenges, and future research directions in characterization methods

The method applied to characterize the physical properties that lead to the figure of merit of a TE material is, in practice, a complicated task, especially at elevated temperatures. The review of commonly adopted techniques for measuring fundamental TE properties in cementitious materials led to the conclusions and challenges summarized below:

- There are two ways by which current can be provided, including AC (alternating current) and DC (direct current) [103]. Using AC for resistance measurement would result in the dipoles of ions being positioned in such a way that they create a path for electric current to flow, thus making a favorable method for resistivity measurements. However, AC measurement takes a non-resistive component called

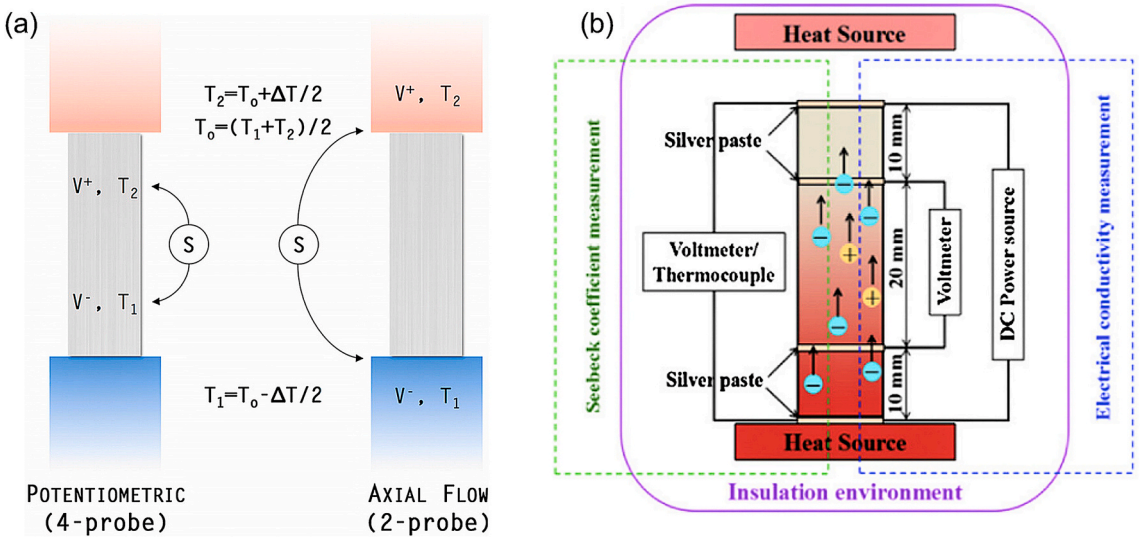

Fig. 7. (a) Potentiometric and axial flow methods for Seebeck coefficient measurements (sourced from Ref. [99]), and (b) an example of Seebeck measurement for TE cement (sourced from Ref. [57]).

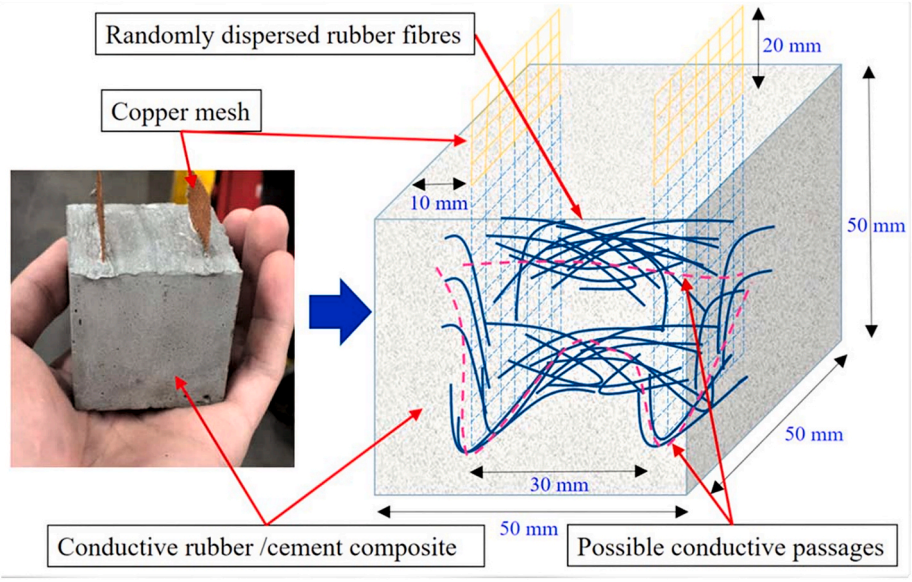

Fig. 8. The schematic of electrical resistance measurement using copper mesh. (source from Ref. [107]).

reactance into account, which results in impedance being measured instead of resistance [62]. The frequency of the AC applied also plays a crucial role in the result [104]. Cementitious materials, however, tend to store electrical charge owing to its capacitive nature. Therefore, it will lead to the generation of a polarization effect, resulting in erroneous values of electrical resistivity [62,103,105], if DC is utilized for measurement. Besides, the moisture content of the sample plays a crucial role in determining whether a sample possesses an insulative or conductive nature.

- Construction materials like concrete and mortars have complicated porous structures. Hence their resistivity values are dependent on their pore size and tortuosity [62]. Oven-dried samples exhibit the resistivity values of up to 10^6 Ω m, while saturated samples have lower resistivity values of around 10 Ω m [106]. The moisture content and age also play a crucial role in determining whether it will exhibit conductive or insulative characteristics. It is because, in cement and concrete samples enhanced with additives like fibers, two ways of electrical conduction are possible, namely electronic and electrolytic. Electronic conduction takes place due to the movement of free electrons in the path formed by the conductive fibers. Electrolytic conduction is observed as a result of the motion of ions present in the porous structure of the samples, which is higher in moist samples. The primary contributor to the TE phenomenon in TE enhanced cement samples is the electronic conduction. Hence, the electrolytic movement of ions needs to be eliminated [105] for evaluating the TE behavior only. It can be done by drying the samples (in the air or the oven).
- Moreover, TE cement has a higher conductivity as compared to ordinary cement due to the additive creating conductive paths inside the cement that can transfer electrons more efficiently [107]. These pathways are unpredictable and vary with the shape and concentration of additives. Therefore, the resistance of materials may exhibit different resistivity due to the form and position of metal contacts used in the measurement. The commonly used metal contacts are in the forms of rods, meshes, and sheets. It has been reported [108] that the contact area of the electrode plays a role in the variability of resistivity measurements (Fig. 8). The resistance measured using a metal mesh will be higher than a rod because the mesh has a larger contact area that increases the possibility of effective conduction paths. To further enhance the contact area and reduce the contact resistance, metal sheet, and silver epoxy can be used to cover the cross-sectional areas of cement samples completely. The geometry of the electrode, therefore, needs to be selected according to the configuration of the real application.
- The transient thermal conductivity measurement method provides quicker results as compared to a steady-state method. Still, the latter is found to have better accuracy and can be conducted at different operating temperatures.
- A reliable Seebeck measurement needs to pay attention to the location of the probes, the thermal and electrical contact, the thermal insulation and electromagnetic shielding, and reliable low electrical signal measurement.

Based on the comprehensive review, the suggested future research directions for characterizing TE cement composites are provided as follows.

- Seebeck coefficient is a parameter usually measured for conventional TE materials. There is no standard measurement method applicable to cementitious materials. A comparative analysis hasn't been carried out to determine out of axial and potentiometric methods, which one leads to higher accuracy. More insightful research is required to find methods for Seebeck measurements suitable for heterogeneous materials like cement composites.
- While developing a cement-based TE material, most researchers have obtained *ZT* value by measuring three key TE properties individually (see Table 1). *ZT* values obtained in this manner are likely to be erroneous as samples used have dissimilar geometry, and individually subjecting them to a temperature gradient can cause huge variations in measurements. Hence, an ideal scenario is to measure the TE properties simultaneously on a single sample so that inaccuracies can be reduced.
- Introducing a temperature gradient into the measurement has shown to result in inaccuracies of up to 50% [101]. A slight inhomogeneity within a sample can result in huge variations of TE properties [102] in the *ZT* measurement. This fact makes it difficult to achieve accuracy and repeatability for the measurements. Reliable measurements are also difficult in materials where sublimation, electrochemical reactions, phase transition, and microstructural evolution is taking place within the material [101].
- There is a requirement of more in-depth studies to find methods suitable to determine the TE properties for cementitious materials,

Table 1
Summary of existing measurement methods used in developing and characterizing cement-based TE materials.

Sample type & size	Seebeck coefficient	Electrical conductivity	Thermal conductivity	Others	Curing conditions	Ref.
Carbon fiber reinforced $40 \times 40 \times 40$ mm^3	Two thermostats measure T Potential meter used to measure V	Two-probe DC	×	×	room temperature 28 days	[86]
Carbon fiber reinforced $75 \times 15 \times 15$ mm^3	Heater: Resistance plate heater Cold side: subjected to ambient Contact: copper foil and silver paint Meter: T-type thermocouple and multimeter	×	×	×	room temperature 100% RH 28 days	[87, 88]
Carbon fiber reinforced $100 \times 100 \times 100$ mm^3	Two thermocouples measure T Multimeter used to measure V	×	×	×	water tank 23 ± 2 °C 28 days	[89]
Carbon fiber reinforced	Heater: Resistance plate heater Cold side: subjected to ambient Contact: copper plate Meter: thermocouple and multimeter $160 \times 40 \times 40$ mm^3	Four-probe DC $160 \times 40 \times 40$ mm^3	Steady-state conduction method 90 mm D & 20 mm H	Power output measurement, SEM	room temperature 95% RH three days	[90]
Carbon nanotube enhanced	Heater: Resistance plate heater (30–100 °C) Cold side: subjected to ambient temperature Contact: silver paste and copper wires Meter: T-type thermocouple and multimeter $40 \times 10 \times 10$ mm^3	Four-probe DC $40 \times 10 \times 10$ mm^3	Laser flash diffusivity method 6.35 mm D & 1~3 mm H	SEM	Pre-cured at 95% RH for 24 h, cured in water for 3 d	[58]
P and N doped carbon nanotube enhanced $40 \times 10 \times 10$ mm^3	Heater: Resistance heater (40–50 °C) Cold side: subjected to ambient Contact: silver paint and copper wire Meter: thermocouple and multimeter	Two-probe DC	×	SEM, TEM, TGA, Raman Spectra	sealed in plastic and cured for 3,7,14, 28 d	[91]
Carbon fiber & expanded graphite enhanced $40 \times 10 \times 10$ mm^3	Fig. 7 (b) Integrated set-up to measure the Seebeck & electrical conductivity under the same temperature gradient.	Four-probe DC T: 33–80 °C.	×	Impact of moisture on S and σ was studied	95% RH for 24 h, cured in water for 3 d	[56]
Expanded graphite enhanced	Fig. 7 (b) Integrated set-up to measure the Seebeck & electrical conductivity under the same temperature gradient. $40 \times 10 \times 10$ mm^3	Four-probe DC T:30–100 °C dT = 5 °C. $40 \times 10 \times 10$ mm^3	Laser flash diffusivity method at room temperature 6.35 mm D & 1–3 mm H	Hall Coefficient	Pre-cured at 95% RH for 24 h, cured in water for 3 d	[57]
Graphene enhanced $10 \times 4 \times 4$ mm^3	samples were subjected to temperature ranges from room temperature to 75 °C & SB coefficient measured using an RZ2001i Ozawa Science equipment	Four-probe DC	thermal diffusivity method T:25–75 °C 20 mm D & 4 mm H	XRD, SEM, EDS, Hall Coefficient	cured at room temperature & dried at 200 °C for 5 h	[59]
Steel fiber-enhanced $75 \times 15 \times 15$ mm^3	Heater: Resistance plate heater Cold side: keep at room temperature Contact: copper foils and silver paint Meter: T-type thermocouple and multimeter	Four-probe DC	×	×	room temperature 100% RH 28 d	[92]
$Ca_3Co_4O_9$ reinforced $160 \times 40 \times 40$ mm^3	Heater: Resistance plate heater Cold side: exposed to ambient Contact: copper plates Meter: T-type thermocouple and multimeter	×	×	XRD, SEM	room temperature 95% RH 3 d	[93]
Fe_2O_3 & Bi_2O_3 enhanced $160 \times 40 \times 40$ mm^3	Heater: Resistance plate heater (up to 90 °C) Cold side: keep at room ambient Thermal contact: copper plates Meter: thermocouple and multimeter	×	×	×	–	[94]
Carbon fiber & Fe_2O_3 particles enhanced $40 \times 10 \times 10$ mm^3	Heater: Resistance plate heater (35–80 °C), a gradient of 5 °C was maintained. Cold side: keep at room ambient Thermal contact: enhanced by silver paste Meter: thermocouple and multimeter	Four-probe DC	Assumed values	SEM	room temperature 95% RH	[97]
ZnO & Fe_2O_3 Nanopowder enhanced	Two thermocouples measure T Multimeter used to measure V $160 \times 40 \times 40$ mm^3	Four-probe DC $160 \times 40 \times 40$ mm^3	Steady-state method $300 \times 300 \times 200$ mm^3	XRD, SEM	cured at standard conditions for 14 d	[100]
MnO_2 enhanced cement with silica fume	Heater: Resistance plate heater (60 °C) Cold side: keep at room ambient Contact: copper sheets & silver adhesive	Four-probe DC $160 \times 40 \times 40$ mm^3	Steady-state conductivity test 75 mm D & 40 mm H	SEM, XRD,	20 ± 1 °C 90 ± 5% RH 28 d	[95]

(*continued on next page*)

Table 1 (*continued*)

Sample type & size	Seebeck coefficient	Electrical conductivity	Thermal conductivity	Others	Curing conditions	Ref.
	Meter: k-type thermocouple and multimeter 160 × 40 × 40 mm^3			EDS, XRF		
ZnO & Al doped ZnO Nano particle enhanced	Heater: Resistance plate heater (up to 85 °C) Cold side: keep at room ambient Contact: copper foils Meter: k-type thermocouple and multimeter 40 × 40 × 40 mm^3	AC impedance measurement 40 × 40 × 40 mm^3	Steady State Longitudinal Guarded method 12.7 mm D & 50 mm H	TGA, SEM & EDX Density measured	ASTM C150, cured for 3,7 & 28 d	[96]
Graphene and ZnO enhanced	SB coefficient measured using an RZ2001i Ozawa Science equipment 4 × 4 × 10 mm^3	Four Probe DC 4 × 410 mm^3	Laser flash diffusivity method & differential scanning calorimeter 17 mm D × 2 mm H	SEM, XRD, EDS	Cured at ambient conditions	[60]

*D represents diameter, and H represents the height of the sample.

especially at elevated temperatures. The time period for which TE behavior is observed in a material, repeatability of the results obtained along with the impact of different operating conditions on the TE performance would be the critical directions in which more research should be conducted in the future.

- It is also important to note that despite there being substantial research on different TE based cement materials, limited work has been carried out in analyzing the impact of key uncontrollable factors like age and moisture on the TE performance of cement composites [56]. More research is needed to assess the impact of these factors on the electrical and thermal conductivity along with the Seebeck coefficient. Quantifying the impact of these factors on the properties would provide a better idea of its suitability as a TE material in the long term. This also helps in determining whether the TE phenomenon observed in enhanced cement composites is a permanent one or something that weakens with time.

4. Composition and performance of TE cement composites at low temperatures

Many experiments have been done on studying the impacts of different compositions and their concentrations for TE cement to obtain a high *ZT*. Three types of additives have been studied, including carbon-based materials, metallic materials, and their combinations. This section reviewed the TE transport performances of the enhanced cement composites at low operating temperatures (under 100 °C) presented in the literature from 1998 to 2020 and the corresponding compositions selected for the composites.

4.1. Carbon-based materials enhanced cement composites

4.1.1. Carbon fiber-enhanced cement composites

Carbon fibers have a diameter of several micrometers [109–111]. They are made of polyacrylonitrile (PAN), pitch, and rayon. The fabrication of PAN-based carbon fibers requires PAN polymer for fiber spinning, followed by oxidative stabilization (200–300 °C) and carbonization (1000–1700 °C) to reduce the impurity [112], so that both electrical and thermal conductivity can be improved [113]. Another commonly used precursor is pitch, which is a by-product of coal and petroleum and is one of the early carbon fiber precursors. The resulting materials usually have lower conductivities than PAN-based carbon fibers [111,114].

In 1998, the TE effect in carbon fiber reinforced concrete (CFRC) was first investigated by Sun et al. [86,115]. The CFRC was made of ordinary Portland cement, short PAN-based carbon fibers, and a disperser. In the experiment, a percolation phenomenon was observed for the Seebeck coefficient and electrical conductivity, where the fiber concentration in the cement composite was in the range of 0.2–2.0 wt%. Percolation results in a sharp step in these properties when the loading of fibers crosses this threshold and results from the establishment of a conductive network of fibers. Below the percolation threshold, there is no continuous network of fibers, and so conduction must occur through both the fibers and the cement medium. The maximum overall Seebeck coefficient of the sample and copper wires was 16.67 μV/K with a mass fiber concentration of 1.0 wt% of cement [115]. The positive Seebeck indicating a hole conduction in CFRC, which could be explained by the quantum tunneling effect when there was almost no connection between fibers, but where the fibers were extremely close together. With an increasing fiber concentration, the continuous fiber matrix improves the hole conduction further [86].

Later, Wen and Chung [87] (1999) determined the Seebeck coefficient of the CFRC itself, without the influence of copper wires. The CFRC was made of isotropic pitch-based carbon fibers and other supplementary cementitious materials (SCM) like silica fume and latex. They found that the plain cement paste had a negative Seebeck coefficient, which represented an intrinsic *n*-type behavior [87]. It contradicted Sun's belief that plain concrete had no TE effect [115]. It is worth mentioning that the reported absolute Seebeck coefficient of the sample was measured relative to copper, which requires subtracting 2.34 μV/K since the copper and the sample were connected in parallel. The test finally showed that the maximum absolute and overall Seebeck coefficients obtained were 5.44 and 3.1 μV/K, with 1.5 wt% fiber and 15 wt% silica fumes inside the CFRC. The result was smaller than what was reported in Sun's work [115], which may be due to the different types of carbon fibers. To enhance the Seebeck coefficient of pitch-based CFRC, the authors used bromine to treat the carbon fiber and studied the effect of bromine-intercalated carbon fibers in CFRC [88]. It was demonstrated that the Seebeck coefficient of the pristine-CFRC was 5.47 μV/K while the bromine-intercalated-CFRC increased to 21.2 μV/K, and it was concluded that higher hole concentrations could be obtained from bromine intercalation.

In 2008, Demirel and Yazicioglu also studied the TE effect in carbon fiber reinforced lightweight concrete, and the impacts of silica fume and fly ash [89]. They found that the Seebeck voltage and thermal conductivity of CFRC decreased with both silica fume and fly ash. As a result, their CFRC exhibited a higher absolute Seebeck coefficient of 127 μV/K without silica fume and fly ash.

Wei et al. [90] investigated CFRC made from sulfate-aluminate cement, PAN-based carbon fibers, etc. The carbon fiber was evenly dispersed into the CFRC using an aqueous dispersion method. This CFRC with 1.0 wt% carbon fiber provided an electrical conductivity, thermal conductivity, and Seebeck coefficient of 0.2 S/m, 0.22 W/mK, and 22.07 μV/K respectively at 27 °C. A *ZT* of 1.33×10^{-7} was first reported for CFRC.

4.1.2. CNT enhanced cement composites

Carbon nanotube (CNT) is another common form of carbon allotrope. CNTs can be classified into various types according to the number

Table 2
Summary of the existing fabrication method and ingredient and TE behaviors of the cement composite.

Type	Cement	Fibers/powders	Chemical Admixture				SCM		Others	Maximum Seebeck	Electrical conductivity	Thermal conductivity	*ZT*	Ref.
			Disperser	Defoamer	Latex	Plasticizing agent	Silica fume	Fly ash		μV/K	S/m	W/mK	–	
Carbon fiber	Portland w/c = 0.3	PAN-based 0.2–1.2 wt%	Compound of cellulose and chloroform	–	–	–	–	–	–	+16.67 (with copper) CF 1 wt%	–	–	–	[86, 115]
	Portland type I w/c = 0.35 or 0.23	Isotropic pitch-based 0.5–1.5 wt%	methylcellulose 0.4 wt%	0.13 v%	0 or 20 wt %	–	0 or 15 wt % SF	–	–	+5.44 1.5 wt% CF + SF	–	–	–	[87]
	Portland type I w/c = 0.35	Bromine-intercalated 0.5–1.0 wt%	methylcellulose 0.4 wt%	0.13 v%	0 or 20 wt %	–	0 or 15 wt % SF	–	–	+5.47 1 wt% CF + SF	–	–	–	[88]
		Isotropic pitch-based 0.5–1.0 wt%							–	+21.2 1 wt% CF + SF				
	Portland CME I 42.5 N	0.5 wt%	methylcellulose 0.4 wt%	0.13 v%	–	+	0 or 10 wt % SF	0 or 15 wt%	Pumice aggregate	+127 0.5 wt% CF	–	–	–	[89]
	P·O.42.5R w/c = 0.34–0.44	PAN-based 0.6–1.0 wt%	Carboxymethyl cellulose 0.08–0.16 wt%	0.05 wt%	–	Polycarboxylate based superplasticizer 0.5 wt%	–	–	Sodium citrate as retarder, 0.1 wt%	+22.07	0.2008	0.22	1.33×10^{-7}	[90]
CNT	P·O.42.5R	CNT d = 10–20 nm L = 5–20 μm	Dry mixing and pressing method							+52.5 15 wt% CNTs, 35 °C	80	0.947	7×10^{-5}	[58]
	Portland w/c = 0.5	*p*-doped CNT *n*-doped CNT 1 wt%	Unknown							−100 −50	0.55 1.9	–	–	[91]
Graphite & graphene	P·O.42.5R	PAN-based CF 1.2 wt%+expanded graphite 5 wt%	Dry mixing and pressing method							−10 60 MPa, 33 °C	0.078	–	–	[56]
	P·O.42.5R	Expanded graphite 5–15 wt%	Dry mixing and pressing method							−20 15 wt% Graphite	2480	3.213	6.82×10^{-4}	[57]
	Portland cement	Graphene 5–20 wt %	Dry mixing and pressing method							34 15%, 70 °C	1168	1.067	4.4×10^{-4}	[59]
	Portland cement	Graphite nanoplatelets & AZO	Dry mixing and pressing method							141.5 10% G+10% ZnO, 70 °C	1390 10%G+10% ZnO, 70 °C	0.99 10%G+10% ZnO, 70 °C	1.01×10^{-2}	[60]
Steel fiber	Portland type I	Stainless steel fiber (d = 60 μm, L = 5 mm) 0.5–1 wt%	–	–	0 or 20 wt %	–	0 or 15 wt % SF	–	–	−63.9 1 wt% CF + SF	3.13×10^{-3}	–	–	[92]
	Portland type I	Stainless steel fiber (d = 60 μm, L = 5 mm) 0–2.5 wt%	–	–	–	–	–	–	–	−59 1 wt% CF	2.08×10^{-3}	–	–	[125]
Metal oxide			–	–	–		–	–		+58.6	–	–	–	[93]

(*continued on next page*)

Table 2 (*continued*)

Type	Cement	Fibers/powders	Chemical Admixture				SCM		Others	Maximum Seebeck	Electrical conductivity	Thermal conductivity	*ZT*	Ref.
			Disperser	Defoamer	Latex	Plasticizing agent	Silica fume	Fly ash		μV/K	S/m	W/mK	–	
	P·O.42.5R w/c = 0.44	$Ca_3Co_4O_9$ powder + PAN 3 wt%				Polycarboxylate based superplasticizer 0.5 wt%			0.10 wt% sodium citrate					
	P·O.42.5R	Fe_2O_3 and Bi_2O_3 microparticles (0.5–5.0 wt%) + PAN	Unknown							+100.28 5 wt% Bi_2O_3	–	–	–	[94]
	P·O.42.5R w/c = 0.23	5 wt% Fe_2O_3 microparticles +1 wt% PAN	–	0.05 wt% (tributyl phosphate)	–	Polycarboxylate based superplasticizer 0.5 wt%	–	–	0.1 wt% sodium citrate + 0–5.0 wt% phenolic resin	+1200	5×10^{-3}	–	8×10^{-4}	[97]
	Portland w/c = 0.46	ZnO (d = 50 nm) & Fe_2O_3 (d = 30 nm) powder 1-5 wt%	–	–	–	–	15 wt % SF	–	–	+3300 5 wt%	1.7×10^{-6}	0.75	7.41×10^{-9}	[100]
	Portland cement	Synthesized MnO_2 nanoparticles 0-5 wt%	–	–	–	Polycarboxylate based superplasticizer 0.6 wt%	15 wt % SF	–	–	−3085 5 wt%	1.88×10^{-4}	0.72	7.60×10^{-7}	[95]
	Portland type I	Nanostructured ZnO and AZO powders (20 nm) 0.2–1 wt%	unknown			Polycarboxylate based superplasticizer 0.4 wt%	Unknown			+0.188 0.4 wt% after 28 d	5.87×10^{-2}	0.6	1.03×10^{-12}	[96]

of graphene layers, including single-wall (SWCNT), double-wall (DWCNT), and multiwall (MWCNT) [116]. Due to the large surface to volume ratio of CNTs, electrons are sensitive to surface-mediated redox reactions, so charge transfer doping is often used to change carrier density and Fermi energy levels [117]. A larger diameter leads to higher electrical conductivities and Seebeck coefficient [118]. By replacing the carbon atoms with other atoms, the electronic properties can be improved.

In 2018, Wei et al. [58] first studied the performance of CNT enhanced cement composites with different CNT concentrations. The composite was made using the dry mixing and compression method instead of the conventional wet mixing method. This dry method enables CNTs to disperse uniformly in the cement matrix without the use of cellulose, resulting in a Seebeck coefficient of 57.98 μV/K, the thermal conductivity of 0.947 W/mK, and higher electrical conductivity of 81.8 S/m. Therefore, a *ZT* as high as 9.33×10^{-5} was obtained in this *p*-type composite.

Another investigation on CNTs reinforced cement nanocomposites was conducted by Tzounis et al., in 2019 [91]. Ordinary Portland cement, 50 wt% deionized water and 1 wt% CNTs were used to prepare the composite with various curing cycles. The experiment found that cement/*n*-CNT nanocomposite with a 14-day curing period performed best with an electrical conductivity of 1.86 S/m and a power factor of 1.44 μW/mK^2. Besides, the dried cement/*p*-CNT and cement/*n*-CNT samples are connected to form a cement-based TEM. When a temperature difference of 10 °C was applied, an output voltage of −0.871 mV was observed.

4.1.3. Graphite enhanced cement composites

Expanded Graphite consists of multi-layers of graphene that can expand by more than 150 times under high temperatures [119]. Since graphite/graphene has no bandgap [120], the electrical conductivity and thermal conductivity become very large. However, these properties are directional, and hence in-plane properties are usually larger than those of the cross-plane.

Wei et al. (2017) [56] introduced a special dry mixing and compression process to prepare expanded graphite/carbon fiber enhanced cement composites. The effect of moisture on TE properties was studied. The results showed that with higher water contents, the better the seebeck coefficient was; 11.59 μv/K at 33 °C at a moisture content of 14.98% along with an electrical conductivity of 78 s/m and power factor of 7.85×10^{-4} W/mK^2 were obtained at a moisture content of 11.44%. Hence, they concluded high moisture content, carrier scattering, polarization effects, and high-density defect interface improve TE performance. This group also studied the TE effect of enhanced cement with expanded graphite in the range of 0–5.0 by wt.% [57]. The compound is also made using the dry method. Expanded graphite/cement-based composites (EGCC) exhibited a distinct TE behavior of an *n*-type semiconductor, with a seebeck coefficient of −20 μV/K and an extremely high electrical conductivity of 2480 S/m. A *ZT* of 1×10^{-4} was achieved at 30 °C, by assuming that the thermal conductivity was maintained at 3.213 W/mK

In 2019, Ghosh et al. [59] used graphene as an additive of cement composite by the dry method. They reported a *ZT* value as high as 0.44×10^{-3}, with 15% graphene at 70 °C. This result is comparable to Wei et al. [56], who also used 15% expanded graphite as the additive. However, graphene is much more expensive than graphite, which increases the cost significantly. Besides, their composite showed a *p*-type TE performance while Wei's group reported an *n*-type TE property for the EGCC.

As shown in Fig. 9, for the carbon fiber enhanced cement composite, the Seebeck coefficient reported in the published paper usually ranges from 5.44 to 22.07 μV/K, except that Demirel and Yazicioglu reported value as high as 127 μV/K [89]. Only a few studies measured the thermal conductivity and electrical conductivity to obtain *ZT*. Carbon fiber is not an ideal candidate for additives to enhance the TE performance of cement. Other carbon-based materials, such as CNT, helps improve the Seebeck coefficient, and graphite/graphene favors higher electrical conductivity, resulting in the overall *ZT* with the order of 10^{-4}.

4.2. Metallic material enhanced cement composites

The abovementioned carbon-based material enhanced cement composites were mostly *p*-type materials (e.g., carbon-fiber, pristine CNT). However, *p*-type materials are not conducive to inter-connecting thermoelectric modules and increasing thermoelectric power. Therefore, *n*-

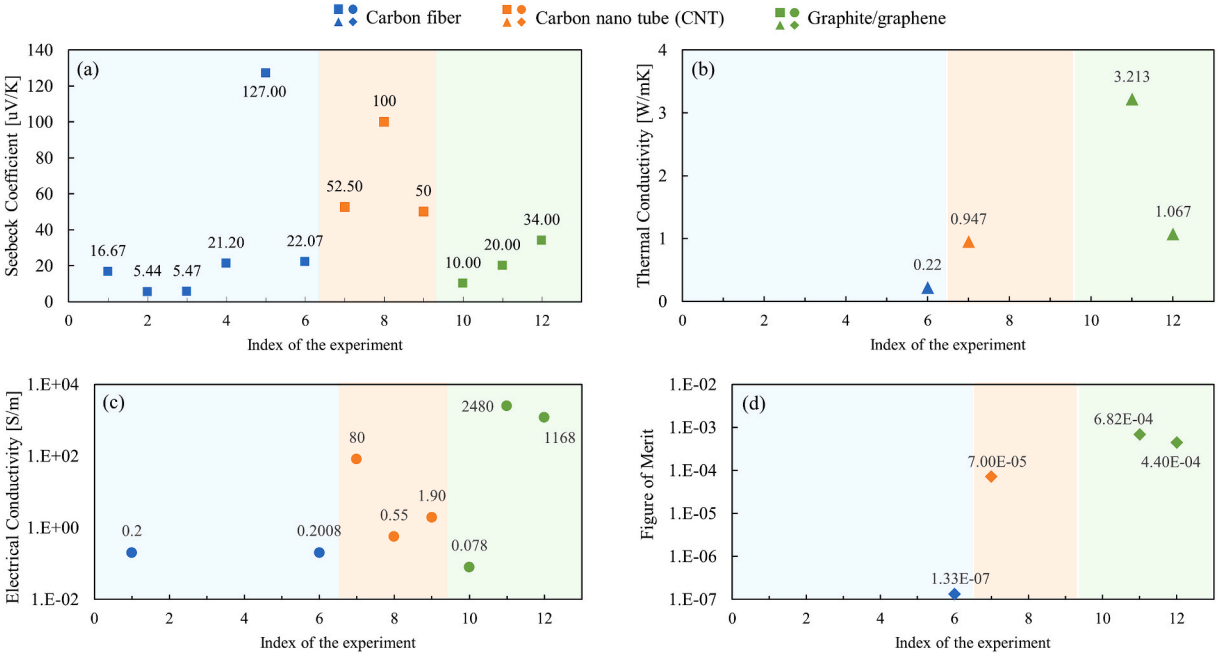

Fig. 9. TE properties of carbon-based material enhanced cement composites: (a) Seebeck coefficient (absolute value), (b) Thermal conductivity, (c) electrical conductivity, and (d) figure of merit *ZT*.

type materials are needed to address this problem. In order to develop an *n*-type cement-based TE, stainless steel fibers with a diameter of 5 mm were used to fabricate a steel-fiber reinforced concrete (SFRC) in Wen and Chung's research [92]. SFRC exhibited a negative Seebeck coefficient of −64 μV/K, with a fiber content of 1.0 wt% of cement. In contrast to the carbon fibers, which contribute to hole conduction, the steel fiber helped the electron movement. The authors designed a thermocouple made by two different types of materials [121] with a *p*-type leg (S = +5.16 μV/K) and an *n*-type leg (S = -48.7 μV/K). They reported a Seebeck coefficient for the whole TEM of 70 μV/K, which is comparable to commercial thermocouples [122].

Ji et al. [100] mixed the nanostructured transition metal oxide (TMO) (e.g., ZnO or Fe_2O_3 powder) into cement composites. Significant enhancement of the Seebeck coefficient (>3000 μV/K) was found. In 2017, the same group synthesized a MnO_2 reinforced cement composite that also produced a very high Seebeck coefficient of −3000 μV/K. The possible explanation offered was an increase in the electron density of states near the Fermi levels of the nanometer metal oxides. However, the material's performance is close to that of an insulator, and its conductivity was very small, ultimately resulting in a low figure of merit. To reduce the high material and processing cost, Ghahari et al. [96] also introduced zinc oxide (ZnO and AZO) nanoparticles to cement slurry. The Seebeck coefficient of their composite was enhanced by 17% because the added nanoparticles reduced hydration reactions. As the density and crystallinity of the material decreased, the thermal conductivity decreased by 9%. As the movement of ions increased, the electrical conductivity also improved and increased by 37% compared with ordinary cement slurry. The maximum Seebeck coefficient of ZnO-cement composite increased from 0.16 to 0.185 μV/K.

The comparison of TE properties between the metallic material enhanced cement composite can be seen from Fig. 10. It has been shown that MnO_2 and ZnO and Fe_2O_3 largely improved the Seebeck coefficient of cement, and the maximum *ZT* as high as 7.6×10^{-7} was obtained in MnO_2 enhanced cement. However, two groups released different orders of ZT on the ZnO enhanced cement, as shown in data points No.4 and No.5.

4.3. Carbon and metallic oxide-based materials enhanced cement composites

In 2013, Wei and his group [93] investigated the impact of metal-oxide powders by mixing micro-sized $Ca_3Co_4O_9$ powders into the PAN-CFRC and obtained the Seebeck coefficient of 58.6 μV/K at room temperature. The reduction of hole activation energy and the increase of the hole concentration of the enhanced composite explained the improvement in TE performance. Then, Wei et al. [94] furthered their work on the TE effect in PAN-CFRC by introducing high-purity Fe_2O_3 and Bi_2O_3 microparticles. As a result, the Seebeck coefficient increased five-fold. When 5.0 wt% Bi_2O_3 was added, a maximum Seebeck coefficient around 100 μV/K was obtained. One possible explanation of the larger Seebeck coefficient could be the appropriate interfacial barrier and the relative content of various interfaces in the composite [94]. The enhancement of TE properties by a thin pyrolytic carbon layer formed at the carbon fiber/cement interface was also investigated by Wei et al. [97]. Five wt.% Fe_2O_3 was introduced into the composite with a measured electrical conductivity of 5 mS/m and a Seebeck coefficient of 1200 μV/K, resulting in a figure of merit of 0.8×10^{-3}. The authors concluded that phonon transport dominated the thermal conductivity. Due to the high concentration of defects in the cement matrix, the phonon relaxation time was reduced, maintaining a low thermal conductivity. Another reason for high TE performance is the appropriate carrier density and the mobility caused by the amorphous structure of the thermally decomposed carbon [97]. The improved TE effects of combining carbon-based and metallic oxide materials attracted the researcher's attention. In 2020, the TE properties of Mayenite/nano-carbon black composites (C12A7/nCB) were investigated [123]. The ionic conductivity was found in order of 5 S/cm of C12A7/nCB with 10% content. The vacancy of oxygen ions as point defect lowers the thermal conductivity. Finally, the *ZT* for 10% C12A7/nCB around $0.01–0.16 \times 10^{-3}$ was reported. Excitingly, the latest literature had shown that the maximum figure of merit of 0.01 could already be obtained when 10% graphene platelets and 10% Al-doped ZnO nanoparticles were introduced into the cement [60]. This is the highest *ZT* that has been found in the TE cement so far, which guided the new trend of the studies on TE cement. The comparison of TE

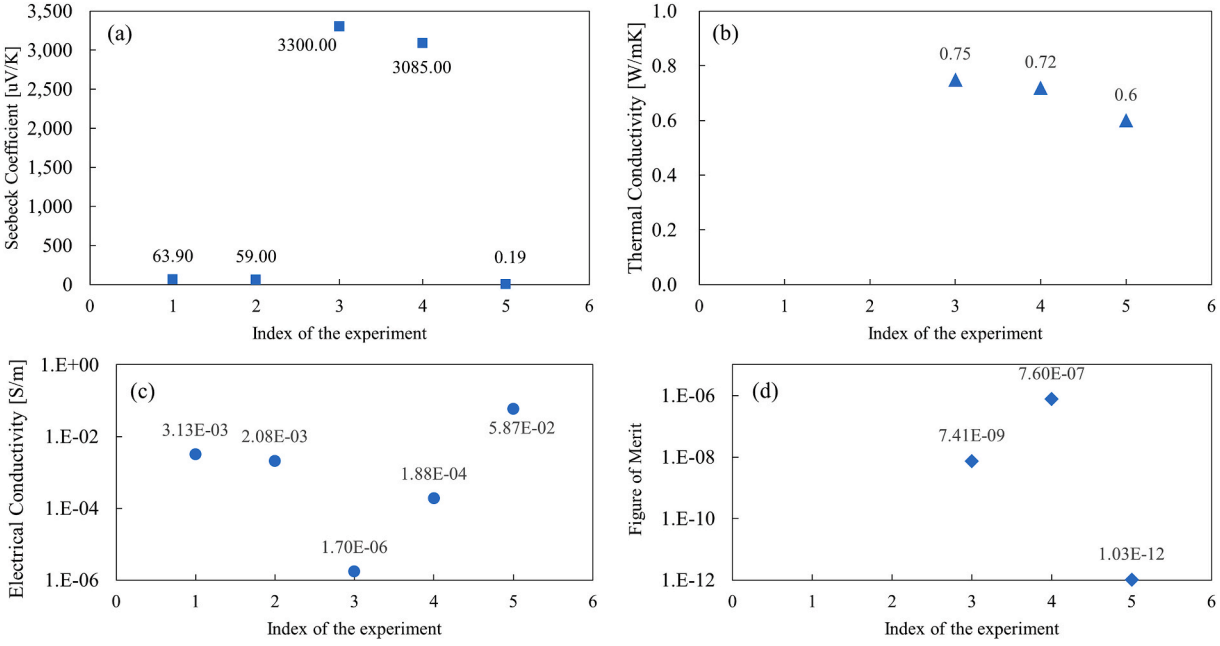

Fig. 10. TE properties of metallic material enhanced cement composites: (a) Seebeck coefficient (absolute value), (b) Thermal conductivity, (c) electrical conductivity, and (d) figure of merit *ZT*.

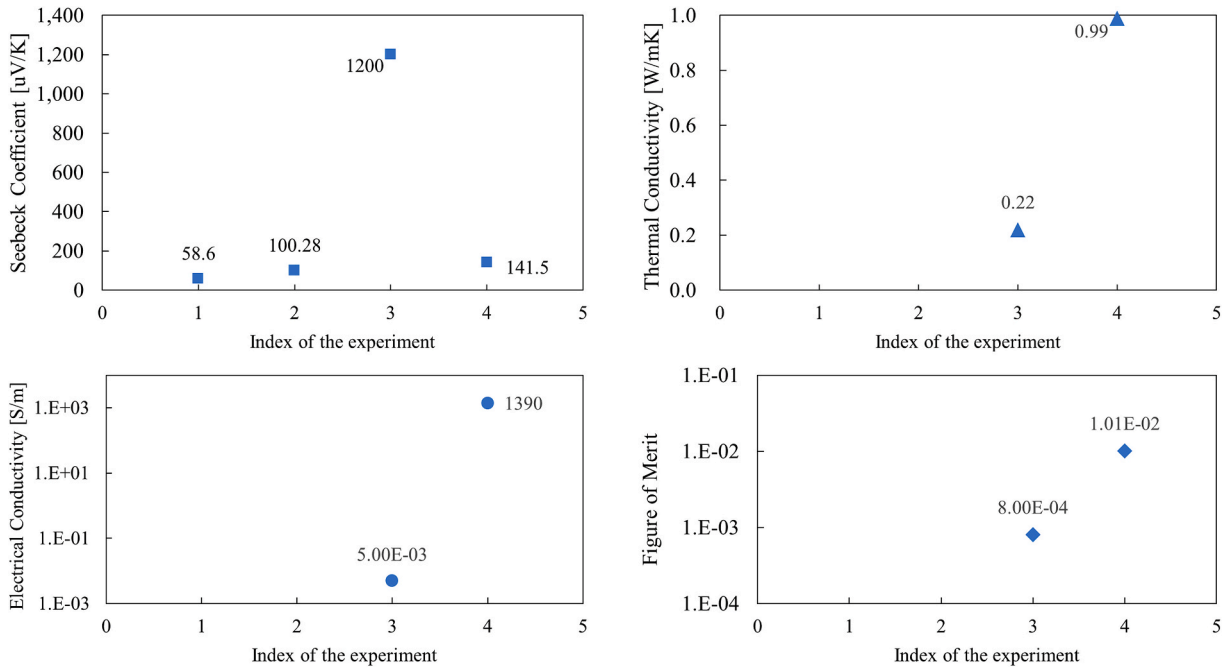

Fig. 11. TE properties of metallic and carbon material enhanced cement composites: (a) Seebeck coefficient (absolute value), (b) Thermal conductivity, (c) electrical conductivity, and (d) figure of merit *ZT*.

properties between the metallic and carbon material enhanced cement composite can be seen from Fig. 11.

4.4. Discussion, challenges, and future research directions in improving TE performances of cement

Table 2 summarizes the fabrication methods, the ingredients used, and the highest TE properties for TE cement composites reported in the literature. Several conclusions can be made based on the summary and comparisons in this section, to guide the selection of methods, materials, and the predicted properties from the empirical analysis.

- The highest Seebeck coefficient was around 3000 μV/K by adding metallic powders (i.e., ZnO, Fe_2O_3, and MnO_2 nanoparticles) [95, 100]. An increased Seebeck coefficient has a contribution to the figure of merit of a TE material. But without enhancing the electrical conductivity and limiting the thermal conductivity, it is not possible to improve *ZT*. Due to the low electrical conductivity, *ZT* of metallic powder reinforced cement is still very small.
- The most effective additives for increasing electrical conductivity in ascending order are steel fibers, carbon fibers, carbon nanofibers, and graphite. Although expanded graphite or graphene-enhanced cement has a low Seebeck coefficient in the order of 10, the electrical conductivity can be significantly improved, resulting in a higher *ZT* with the order of 10^{-4}.
- Usually, high electrical conductivity and the Seebeck coefficient cannot be obtained at the same time. Hence, most of the TE cement composites had a *ZT* within the order of 10^{-4}–10^{-3}, as shown in Fig. 12. However, the latest research had shown that *ZT* is improved to 10^{-2} at 70 °C when 10% graphene and 10% Al-doped ZnO nanoparticles were introduced into cement. This composite has a Seebeck coefficient of around 141 μV/K while maintaining a high electrical conductivity of around 1390 S/m.
- In contrast, most of the resultant materials have a *ZT* limited to the range of 10^{-3} to 10^{-7}, which is insignificant in comparison to the commercially available thermoelectric materials ($ZT = 1$).
- In addition to composition selection, other challenges for cement-based composites include heterogeneity, porosity, and brittleness.

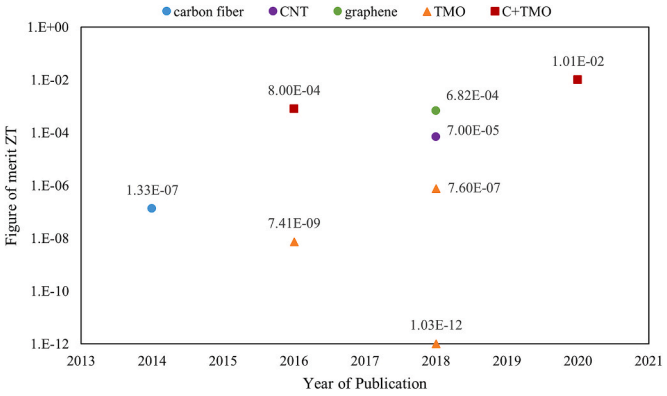

Fig. 12. The historical data of ZT for TE cement composites using different additive materials.

Wei et al. studied the effect of porosity and microcracks on the TE properties of the cement matrix composites [124]. The highest conductivity, power factor, and *ZT* were obtained when the porosity was 3.9%, as compared with 10.7% and 28.9%. Pores and cracks affect the Seebeck effect and meanwhile reduce the conductivity. However, the Seebeck effect for expanded graphite and CFRC is enhanced when the crack is at a 90-degree angle to the heat flow direction.

- The continuous search for possible TE cement composites with higher *ZT* is critical to obtain cement-based TE materials with comparable thermoelectrical performance. However, there is limited research theory to guide the selection of additives. A new trend observed from the recent publication is the combination of graphite/graphene and metallic oxide additives. Also, doped additive materials may bring the improvement of TE performance. It is vital to investigate on the graphite/graphene and doped metallic oxide enhance cement for performance verification and obtaining better TE cement.
- Although many cement composites show the *p*-type TE properties, the number and the performance of *n*-type TE cement are still very

low. N-type and *p*-type TE materials can be connected in series electrically and thermally in parallel to form TE couples, and a large number of TE couples forms TE module, which helps improve the total cooling/heating capacity or total power output. The lack of available *n*-type materials makes the cement-based TE element difficult to expand. Therefore, develop *n*-type TE cement with compatible TE properties is of significance in manufacturing the cement-based TE module.

5. Modeling methods for TEM design and performance evaluation

Additional valuable insight supplementing the experimental characterization of TE cement and the evaluation of its performance under operating conditions can be gained via theoretical and computational modeling approaches. There are two main advantages of developing TEM models: firstly, they help accelerate and optimize the design and, secondly, they provide a deeper understanding of the properties of the materials under consideration, helping to guide modifications at a microscopic level that improve the TE characteristics, and hence the performance of devices at a macroscopic level. These considerations point to the necessity of developing a multi-scale modeling framework, in which information obtained at the microscopic scale is then used to parameterize models at the meso- and macroscopic scale. Typically, one can calculate TE parameters at the atomistic level, and then these can be used in meso- and macroscopic heat and charge transport equations.

In this section, the materials design aspect, going from atomistic modeling approaches towards macroscopic models, is reviewed. It will first describe how classical and quantum mechanical atomistic simulations have been used to model the structural and electronic properties of materials, and then how these have been used to determine their TE properties. Next, simple models that have been developed to calculate the TE properties of composite materials based on those of the individual components will be described in 5.2–5.3. The next subsections then focus on some device performance evaluation aspects, with summarizations of previous works in the literature for single TE leg, TE pair, and TEM. To this end, models need to incorporate a variety of physical phenomena. The minimum requirement is to include a description of heat transport, temperature-dependent physical properties, and the Thompson effect. The next level of sophistication involves the introduction of charge transport and variable electric fields. Together, the relevant partial differential equations constitute a set of governing equations that must be solved simultaneously (and due to their complexity, solved numerically) for a representative problem geometry either in steady-state or out-of-equilibrium (transient) conditions. This approach can be used not only to assess the properties of a device but also to interpret experimentally measured TE properties by modeling the actual experimental setup.

5.1. Atomistic modeling: structural, electronic, and thermodynamic properties of materials

A valuable tool to supplement experimental investigations in the search for new thermoelectric materials is atomistic modeling. The goal of this approach is to predict materials properties from purely theoretical considerations, the success of which can be verified by experimental techniques. While experiments measuring materials properties are conducted in the macroscopic world, atomistic modeling considers the material as a collection of atoms interacting via empirical potentials or *force fields*. Due to the complexity of the interactions, these models are generally studied using computer simulation, e.g., molecular dynamics, and are hence limited in size (or the number of atoms) and simulation time. With present-day respectable computational resources, one can study models made of millions of atoms ($10 \times 10 \times 10$ nm^3) for times, reaching up to microseconds. Macroscopic properties are then computed by extrapolating to larger sizes and by averaging over time, in a way that mimics the experimental situation. A caveat is that experimental timescales are usually much longer than simulation timescales (minutes vs. microseconds). The assumption is that both access the thermodynamic averages [126].

The *force field* approach describes interatomic forces that depend on the distances, angles, torsions, and partial charges between atoms in the case of ionic systems. Unless already available, the development of force fields is a daunting task that has to be carried out for every specific material. A more attractive strategy is to use *ab initio* or *first-principles* methodologies that only rely on the knowledge of the atomic species of which the material is made of. A particularly useful such approach is density functional theory (DFT), which allows for the determination of interatomic forces by solving the quantum mechanical equation for the electronic density [127]. The achievement of this higher accuracy comes at the cost of having to reduce the size of the systems to a few thousand, and sometimes just hundreds of atoms. Additionally, molecular dynamics simulations are reduced to times of the order of a few picoseconds.

First-principles approaches are useful to obtain information on structural properties of the material like interatomic distances and angles, lattice parameters, and elastic moduli (mechanical properties) as well as vibrational and thermal properties in the harmonic regime. They also give access to electronic properties such as energy bands and density of states, which are necessary to compute the thermoelectric transport coefficients via Boltzmann's equation, as will be shown in the next subsection. First-principles calculations have been carried out for a variety of cement analogs that are representative of C–S–H gel. These are known minerals described by relatively small, ordered unit cells like tobermorite [128] and jennite [129,130] corresponding to different C/S ratios and hydration levels. Recently, first-principles calculations were used to study the stability of cement as a container for radioactive waste [131] and to analyze the formation of H_2 due to radiolytic processes [132].

Force-field methods access a larger scale and are useful to study systems that include point and extended defects like dislocations, voids, surfaces, and grain boundaries, and to model diffusion and thermodynamic properties like free energies beyond the harmonic regime. Force fields can also be used to obtain thermal transport properties like the lattice thermal conductivity [81], which is necessary to compute the TE figure of merit *ZT*. Since they can access superstructures with a larger number of atoms, they become particularly important to describe defective systems like C–S–H gel. There are many works devoted to the development of C–S–H models that are consistent with experimental data. They construct supercells with ordered motifs like tobermorite (low C/S ratio, around 0.8) and jennite (high C/S ratio, around 1.5), and modify them by replacing Si with Ca, breaking the silicate chains, and introducing water, for achieving higher C/S ratios. They are designed under the constraint of reproducing a C/S ratio close to the experiment, i.e., between 1.5 and 1.7, and to reproduce the desired hydration levels. In the past few years, there have been several new models proposed based on molecular dynamics simulation using force fields that have found good acceptance in the community [133–135]. These models involve a larger number of atoms in the unit cell, ranging from 500 to 3500. Many force fields can describe the interatomic interactions in cementitious materials, including CLAYFF [136,137], INTERFACE [138], CSH-FF [139], and others [140,141].

To the best of our knowledge, there are no published works, neither first-principles nor using force fields, focusing on computing TE properties of cementitious materials. It is, therefore, worth exploring this research direction, as it allows for the possibility to assess the effect of modifying the material, e.g., by doping, on the TE properties without the need to fabricate samples. This approach can provide indications of possible routes to improve the properties of the TE materials. More recently, several groups have been attempting to design new TE materials using machine learning techniques that do not rely on gaining a deep understanding of the material but on an intensive data analysis

approach [142].

The next step in this hierarchy of techniques is to bridge the atomistic description with the continuum to address meso- and macroscopic length and time scales. Here, rather than following the motion of individual atoms, the material is described in terms of (continuous) particle and charge densities and temperature and electromagnetic fields, whose evolution is governed by a set of coupled partial differential equations, as described later in this section. But before that, the approach to obtain TE transport coefficients from first-principles calculations and molecular dynamics simulations are summarized.

5.2. Thermoelectric transport properties: the Boltzmann transport equation

The Boltzmann transport equation (BTE) is useful for gaining insight into the microscopic transport properties of real materials. The electronic transport coefficients are related to the electronic band structure of material [100]. A widespread assumption is that, after the action of an external perturbation, the relaxation to equilibrium is exponentially fast, with a time constant (relaxation, or scattering time) denoted by τ. It is known as the relaxation-time approximation and is important for solving the BTE in practical terms [143,144]. In the relaxation-time approximation, the electronic transport coefficients are related to the integral over the Brillouin zone of the squared band velocities, $v_{b,k}$, multiplied by the scattering times $\tau_{b,k}$, where the subscripts b and $\boldsymbol{k}$ run over the band and Brillouin zone indices, respectively. The relevant quantities for describing the thermoelectric properties of a material are the moments of the generalized transport coefficients, known as Onsager's coefficients L_n, which are computed as [145]:

$$L_n(E_F,T) = \frac{e^2}{4\pi^3}\sum_b \int v_{b,k}^2 \tau_{b,k}\left(\varepsilon_{b,k}-E_F\right)^n \left(-\frac{\partial f_0}{\partial E}\right) dk, \quad n=0,1,2 \tag{5.1}$$

where $\varepsilon_{b,k}$ indicate the energy bands and f_0 is the equilibrium energy distribution given by Fermi-Dirac's statistics. These scalar coefficients are valid for an isotropic material, but they can also be generalized to tensor coefficients in the case of anisotropic crystalline materials. These coefficients enter into the linear constitutive equations for the electric and heat currents (J_e and J_q, respectively) flowing through the sample:

$$\boldsymbol{J}_e = L_0\boldsymbol{E} + \frac{L_1}{eT}(-\nabla T) \tag{5.2}$$

$$\boldsymbol{J}_q = \frac{L_1}{e}\boldsymbol{E} + \frac{L_2}{e^2T}(-\nabla T) \tag{5.3}$$

where, $\boldsymbol{E}$ is the external electric field. In Eqs. (5.2) and (5.3), it is assumed that there is a uniform charge density across the sample. As a consequence, the gradient of the chemical potential can be neglected. However, this may not be an accurate approximation at the interface between different phases. One such interface could be between cement and an additive material where there may be an accumulation of space charge.

There are two typical experimental conditions: zero temperature gradient ($\nabla T = 0$) and zero current density or open circuit ($\boldsymbol{J}_e = 0$). Under these conditions, the electrical conductivity σ, Seebeck coefficient S, and electronic thermal conductivity κ_e are defined as:

$$\sigma = L_0, \cdot S = \frac{1}{eT}L_1L_0^{-1} and, \kappa_e = \frac{1}{e^2T}\left(L_2 - \frac{L_1^2}{L_0}\right) \tag{5.4}$$

In the constant relaxation time approximation, where $\tau_{b,k} = \tau$ is energy-independent, the Seebeck coefficient becomes independent of τ and can be obtained as a function of doping and temperature in a single scan [143].

Nowadays, the determination of these coefficients has been implemented in computer codes of free distribution like BoltzTrap [146] and BoltzTraP2 [147]. These codes have been used for a variety of materials, but not cementitious ones so far. Two of the closest ones are oxides like $SrTiO_3$ derivatives [148] and Cobaltates [149]. It is then of interest and value to apply this methodology to compute the TE properties of cement analogs, as described in the previous section.

5.3. Lattice thermal conductivity

The only missing ingredient to compute the figure of merit, ZT, is the lattice thermal conductivity, κ_{lat}. This can be obtained in two ways. One is by computing phonon dispersions at the first-principles level, and then solving the Boltzmann equation for phonons, e.g., using the ShengBTE software [150]. The calculation of first-principles phonons is computationally quite demanding, and only feasible for system sizes up to one-two hundred atoms. Beyond this, it becomes impracticable, thus excluding systems with large unit cells like some recent models of cement. The second one is to construct (or use) a classical force field and compute κ_{lat} via molecular dynamics (MD) simulations. It can be done for systems made of up to a million atoms, which are still within the nanometer-size range. These allow for analyzing the effect of point defects and grain boundaries. Still, they quickly find limitations for composite phases, as force fields should be developed for specific combinations of materials to supplement those already available for cementitious materials. A comparison showing that the results obtained using BTE and MD are in the satisfactory agreement has been presented very recently [151]. In the case of disordered and porous cementitious materials, since κ_{lat} is already low (for cement it is around 0.5 W/mK), already similar to κ_e., it is a legitimate question whether or not it is worthwhile to investigate on further lowering it.

5.4. Composite materials: effective medium theory and beyond

Cement (and more generally concrete) is a highly heterogeneous material made up of many components. Some of them are in cementitious phases with varying degrees of C/S ratio and water content (tobermorite, jennite). Others are unreacted components like quicklime and silica, or other components like carbonates, aluminates, sulfates, and ferrites. In the case of concrete, one has also to consider aggregates like sand and gravel. Finally, one needs to consider additives. These include hydration retarders and accelerators, plasticizers, and corrosion inhibitors, which generally appear in small proportions. Other additives frequently used that will feature in higher proportions cost-effective fillers like fly ash, carbon fiber, and blast furnace slag. Of particular relevance to this review are also additives that improve TE properties like the TE materials Bi_2O_3 and Bi_2Te_3. It is, therefore, essential to be able to calculate the TE properties of such composite media based on the properties of the individual components. It is precisely what the Effective Medium Theory (EMT) does through a set of approximations [152,153]. The effective (electronic or total) thermal conductivity κ_{eff} and the effective electrical conductivity σ_{eff} are given by the numerical solution of the following simultaneous equations:

$$x_1\frac{\kappa_1-\kappa_{eff}}{\kappa_1+2\kappa_{eff}} + x_2\frac{\kappa_2-\kappa_{eff}}{\kappa_2+2\kappa_{eff}} = 0 \tag{5.5}$$

$$x_1\frac{\sigma_1-\sigma_{eff}}{\sigma_1+2\sigma_{eff}} + x_2\frac{\sigma_2-\sigma_{eff}}{\sigma_2+2\sigma_{eff}} = 0 \tag{5.6}$$

where x_1 and x_2 are the volume fractions of the individual components in the composite and $x_1 + x_2 = 1$. This model can be easily generalized to more than two components and applied to obtain effective transport properties for cementitious materials, as mentioned above. The effective Seebeck coefficient (S_{eff}) is obtained by applying the EMT formalism to the entropy flux density and the chemical potential, which gives the equation below [154]:

$$x_1\frac{\frac{\kappa_1}{S_1}-\frac{\kappa_{eff}}{S_{eff}}}{\frac{\kappa_1}{S_1}+2\frac{\kappa_{eff}}{S_{eff}}}+x_2\frac{\frac{\kappa_2}{S_2}-\frac{\kappa_{eff}}{S_{eff}}}{\frac{\kappa_2}{S_2}+2\frac{\kappa_{eff}}{S_{eff}}}=0 \tag{5.7}$$

where the thermal conductivities correspond to the electronic contribution. In practice, only the total thermal conductivity $\kappa_{tot} = \kappa_e + \kappa_{lat}$ is measured, and the Wiedemann-Franz law gives an indirect way to assess the electronic and lattice components [82].

While the relative simplicity of the EMT is attractive, it must be recognized that EMT is a parameter-free theory that treats the medium as being homogeneous. As a consequence, the solution of these equations yields a percolation threshold, i.e., a critical concentration $x_1 = x_c$ below which there is no electrical conduction when the first component is metallic and the second one is insulating, of $x_c = 1/3$. However, it has been shown in experiments with cement composites, such as carbon-fiber impregnated cement, that percolation occurs at a volume fraction as low as 0.5 vol% [155]. A variant of the EMT, the Generalized Effective Medium Theory (GEMT), extends the validity of the approximation to mixtures with a percolation threshold. The price to pay is that two additional parameters are introduced, α and t, which must be fitted. The equations to be solved simultaneously become:

$$x_1\frac{\kappa_1^{1/t}-\kappa_{eff}^{1/t}}{\kappa_1^{1/t}+\alpha\kappa_{eff}^{1/t}}+x_2\frac{\kappa_2^{1/t}-\kappa_{eff}^{1/t}}{\kappa_2+\alpha\kappa_{eff}}=0 \tag{5.8}$$

$$x_1\frac{\sigma_1^{1/t}-\sigma_{eff}^{1/t}}{\sigma_1^{1/t}+\alpha\sigma_{eff}^{1/t}}+x_2\frac{\sigma_2^{1/t}-\sigma_{eff}^{1/t}}{\sigma_2^{1/t}+\alpha\sigma_{eff}^{1/t}}=0 \tag{5.9}$$

$$x_1\frac{\left(\frac{\kappa_1}{S_1}\right)^{1/t}-\left(\frac{\kappa_{eff}}{S_{eff}}\right)^{1/t}}{\left(\frac{\kappa_1}{S_1}\right)^{1/t}+\alpha\left(\frac{\kappa_{eff}}{S_{eff}}\right)^{1/t}}+x_2\frac{\left(\frac{\kappa_2}{S_2}\right)^{1/t}-\left(\frac{\kappa_{eff}}{S_{eff}}\right)^{1/t}}{\left(\frac{\kappa_2}{S_2}\right)^{1/t}+\alpha\left(\frac{\kappa_{eff}}{S_{eff}}\right)^{1/t}}=0 \tag{5.10}$$

The percolation critical volume fraction x_c is given by $x_c = 1/\alpha + 1$. For $\alpha = 2$ and $t = 1$, the GEMT reduces to the EMT, giving a percolation threshold of 1/3. For any other values, the percolation threshold will be different. The GEMT provides a simple way of addressing the consequences of additives being organized (and in the case of fibers, directionally organized) within the cement matrix, rather than homogeneously dispersed.

The problem with this approach is that the parameters α and t can be determined by fitting the above expressions to experimental data, but it is difficult, if not impossible, to derive them theoretically and, hence, the predictive power of the GEMT is quite questionable. It is, therefore, of great interest to explore the possibility of determining these parameters from simulations by considering particles of varying size, shape, and orientation.

5.5. Macro-scale modeling methods for performance evaluation of TEM

TE cement could be potentially applied to the power generation, air conditioning, and sensing system in buildings. Hence, developing models to evaluate the performance of TEM is of considerable significance to accelerate and optimize the design. This sub-section summarizes the previous modeling works in the literature for single TE leg, TE pair, and TEM. Macroscale modeling for this application starts by incorporating different physical phenomena considered to be of interest. At a minimum, this must include a description of heat transport, temperature-dependent physical properties, and the Thompson effect. Additional physics, such as variable electric fields, etc., can be included to increase the sophistication. Together, the relevant partial differential equations constitute a set of governing equations that must be solved simultaneously (and due to their complexity, solved numerically) for a representative problem geometry at either representative steady-state or out-of-equilibrium (transient) conditions.

5.5.1. General governing equations

5.5.1.1. A simplified model for a TE leg. Fig. 13a shows a single *n*-type TE leg with a length *L*. The two terminals of the TE leg are in thermal and electrical contact with metal and connected in series with a battery. Power input with a voltage *V* is applied to the TE leg and the current *I* is generated in the closed circuit. In this scenario, the TE leg operates as a TEC/TEH. The heat transport inside the TEC/TEH includes the Seebeck-Peltier effect, Joule heating, and Fourier's law of conduction. The direction of the Peltier heat is related to the difference in the electrochemical potential of the TE and contact materials. From the fundamental theory described in Appendix, it can be concluded that heat due to Seebeck-Peltier heating (excluding the Thomson effect) is released at the junction when the current flows from the metal to the *n*-type TE material. Heat due to Seebeck-Peltier cooling (excluding the Thomson effect) is absorbed in the junction when the current flows from the *n*-type TE to the metal contact. For a *p*-type TE material, the situation is the opposite.

This simplified model has been largely used in system-level modeling because it is simple and easy to integrate with other sub-models and therefore reduces the computation time as compared with finite element models using commercial software [22,156]. Several assumptions are made to simplify the TE model:

- The material properties are independent of temperature;
- The Thomson effect and the surface heat losses contribute equally to the extremes of the TE element;
- The thermal and electrical resistances of the metal contact are negligible;
- The model is one-dimensional (1D) and at steady state.

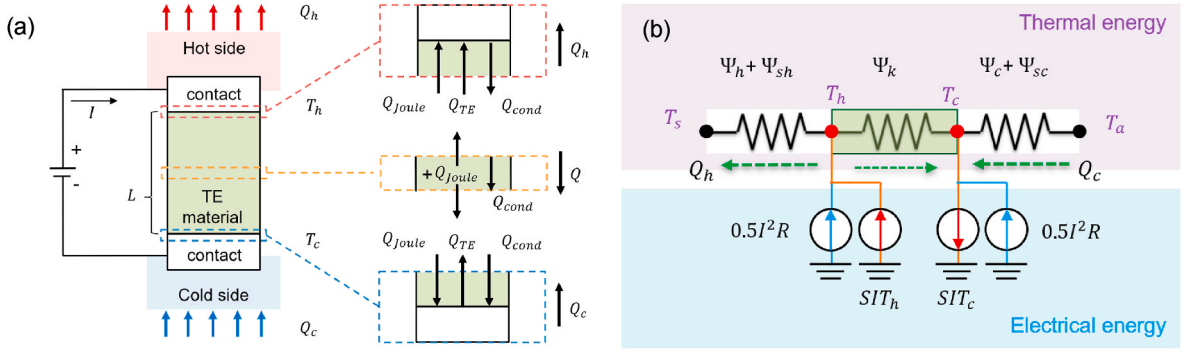

Fig. 13. (a) The schematic diagram of a single thermoelectric leg with power supplied, and (b) the thermal-electrical analogy resistance network (Figures were reproduced from Ref. [157]).

For the most simplified models, the problem is reduced to a thermal resistance network problem, as shown in Fig. 13b. Only the temperatures of particular nodes and three thermal effects, including Fourier's law of heat conduction, Joule heating, and Seebeck-Peltier heating/cooling, are considered in the TE element. According to the energy conservation, the heat released on the hot side equals the heat pumped by the Peltier effect and the heat generated by Joule heating while excluding the heat diffusing down the thermal gradient in the TEC. The next step in improving a simple model is to include the Thomson effect ($\tau I\Delta T$) and the surface heat loss (Q_{loss}). Then the heat equation at the hot side can be written as [159]:

$$\dot{Q}_h = SIT_h - K(T_h - T_c) + \frac{1}{2}I^2R + \frac{1}{2}\tau I\Delta T + \frac{1}{2}\dot{Q}_{loss} \tag{5.11}$$

For the cold side, the heat extracted from the ambient equals the heat generated by the Peltier effect, excluding the heat transport by the thermal gradient and that generated by Joule heating in the TEC. Then the governing equation at the cold side considering Thomson effect and surface heat loss can be modified to Refs. [159]:

$$\dot{Q}_c = SIT_c - K(T_h - T_c) - \frac{1}{2}I^2R - \frac{1}{2}\tau I\Delta T - \frac{1}{2}\dot{Q}_{loss} \tag{5.12}$$

As shown in Fig. 13, the electrical power applied to the TEC is used for Joule heating and increases the electrochemical potential at the hot side. It is also the power difference of heat between the hot and cold sides. After considering the Thomson effect and surface heat loss, the electrical power can be written as

$$P = \dot{Q}_h - \dot{Q}_c = SI(T_h - T_c) + I^2R + \tau I\Delta T + Q_{loss} \tag{5.13}$$

The coefficient of performance (COP) is the ratio of useful heating or cooling power provided to work required ($COP = \dot{Q}/P$) with higher values resulting in lower operating costs. It is found that higher ZT leads to a better COP [160], and for a given ZT, a higher COP can be obtained with a smaller temperature difference [161]. The maximum COP of a TEC can be simplified to the relationship between operating temperatures and ZT [162,163]:

$$COP_{max} = \frac{T_c}{\Delta T}\frac{\sqrt{1+ZT} - \frac{T_h}{T_c}}{\sqrt{1+ZT}+1} \tag{5.14}$$

5.5.1.2. A simplified model for a TEG. When applying the temperature difference at the two sides of the TE leg, the TEG will generate power/output voltage. Unlike the TEC and TEH, the hot end of TEG absorbs heat from the source, while the cold end exudes heat from the sink as shown in Fig. 14. As discussed in Appendix, in *n*-type TEG, the hot-side interface absorbs heat (due to Seebeck-Peltier cooling excluding the Thomson effect), and the cold-side interface releases heat (due to Seebeck-Peltier heating excluding the Thomson effect) when electrons move from the hot side to the cold side. But for a *p*-type TEG, the direction of Seebeck-Peltier heating and cooling is the opposite.

In the case of TEG, the heat absorbed from the heat source and generated by the Joule effect are consumed in the Seebeck effect and transferred to charge carriers, leading to a potential difference. The governing equation at the hot side can be modified as Eq. (5.15) after considering the Thomson effect \and heat loss [159]:

$$\dot{Q}_h = SIT_h + K(T_h - T_c) - \frac{1}{2}I^2R + \frac{1}{2}\tau I\Delta T + \frac{1}{2}\dot{Q}_{loss} \tag{5.15}$$

The total heat released at the cold end is the sum of the heat generated by transferring electrons in the Seebeck effect, by the Joule effect, and by heat conduction. The governing equation at the hot side can be modified as Eq. (5.16) after considering the Thomson effect and heat loss [159].

$$\dot{Q}_c = SIT_c + K(T_h - T_c) + \frac{1}{2}I^2R - \frac{1}{2}\tau I\Delta T - \frac{1}{2}\dot{Q}_{loss} \tag{5.16}$$

Thus, the difference of thermal power between the hot and cold sides is the power generated in a TEG. After considering the Thomson effect and surface heat loss, the electrical power can be written as

$$P = \dot{Q}_h - \dot{Q}_c = SI\Delta T - I^2R - \tau I\Delta T - \dot{Q}_{loss} \tag{5.17}$$

The power efficiency or the energy conversion efficiency is the ratio of power generated to the heat absorbed at the hot side, which is given by $\eta = P/Q_h$. It is shown that a larger ZT results in higher efficiency, and a smaller temperature difference leads to a better efficiency [164]. The energy conversion efficiency can also be simplified to the relationship between operating temperatures and ZT [165]:

$$\eta = \frac{\Delta T}{T_h}\frac{\sqrt{1+ZT}-1}{\sqrt{1+ZT}+\frac{T_c}{T_h}} \tag{5.18}$$

In the simplified model, the material properties are usually independent of temperature. However, this might not be true when the TEM working under a large temperature difference or its material properties are very sensitive to the temperature. Naveed and Mubashir [166] carried out a sensitivity analysis for a solar TEG to study the percentage change for responding per 10% change in the parameter value. The result showed that the power output is most sensitive to the thermal conductivity among the four selected properties, followed by the Seebeck coefficient, convection coefficient at the cold side, and electrical resistance.

In addition, this simplified model is one-dimensional. So, it works better for the TE leg with the regular cuboid shape rather than the cone shape with varying diameters along the length or other irregular geometries. The 1D model cannot present the temperature profiles along the TE leg accurately but only gives the heat transferred to the

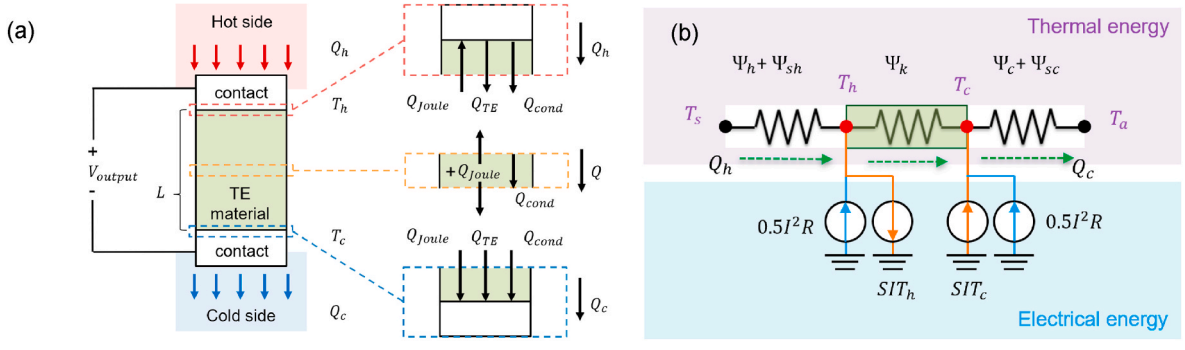

Fig. 14. (a) The schematic diagram of a single thermoelectric leg with applied temperature difference and voltage output, and (b) the thermal-electrical analogy resistance network (Figures were reproduced from Ref. [157]).

surroundings. Since it only considers the steady-state performance, the model is no longer applicable to the system with transient reactions.

The fourth term in Eqs. (5.11)–(5.12) and Eqs. (5.15)-(5.16) is heat transport due to the Thomson effect. This term exists when the Seebeck coefficient is varied with different temperatures. It was found that the Thomson effect can lower the efficiency and power output of a TEG using Bi_2Te_3 significantly, especially when the current output is large [167,168]. But when $\tau I/K \ll 1$, the influence of Thomson effect becomes negligible [168]. For a TEC, when the ZT_c is smaller than the ratio of Seebeck coefficient to Thomson coefficient, most of the heat due to the Joule effect can be absorbed by the Thomson effect on the cold side and carried to the hot side through the current [169]. Therefore, the Thomson effect changes the temperature profiles and increases the cooling power of the TEC.

The fifth term in Eqs. (5.11)–(5.12) and Eqs. (5.15)-(5.16) is the surface heat loss, mainly containing convective and radiant heat losses. The convective heat loss from the surface to the surrounding affects the temperature profile. For a small temperature-difference system (ΔT = 40–80 K) with an ambient temperature of 298 K, the impact of convection loss, with a convective coefficient of 0–100 W/m^{2}K, on the energy conversion efficiency of a TEG, can be ignored [170]. But for a large temperature-difference system (T_h=700 K, T_c = 300 K), The heat loss on the surface causes more heat input of the TEG to flow to the surface than to be converted into electricity power, greatly affecting the efficiency even when the convective coefficient is between 0.1 and 20 W/m^{2}K [171].

5.5.1.3. Complex models. A more complex model is needed to overcome the abovementioned limitations of the simplified model and obtain more accurate and detailed results of temperature profiles and energy transport with the response to time. The multidimensional (2D or 3D) governing equations for both the thermal field and electromagnetic field are presented in this section.

The multidimensional heat equation follows the energy conservation of the TE leg and is described in the form of a partial differential equation (PDE). The volumetric heat sources in a TE leg are summarized in Table 3.

The first item in Table 3 is the Fourier's law of heat conduction for a unit control volume of TE leg. It is the difference of conduction heat between two or more sides of the control volume. The second term is Joule heat per volume where $\boldsymbol{J}_e$ is the electrical charge density ($\boldsymbol{J}_e = I/A$) and σ is the electrical conductivity ($\sigma = L/RA$). The third term is the Seebeck-Peltier heating or cooling per volume. It is the product of charge density, temperature, and the derivative of the Seebeck coefficient with respect to space. In some cases, the Peltier term is included in the heat governing equations, but for other cases, the Peltier term is considered at the TE-metal interface. The difference between the two approaches of treating the Peltier term only occurs when the Seebeck coefficient inside the TE material has a spatial dependence. Otherwise, the term $\nabla S \cdot \boldsymbol{J}_e T$ is zero inside the TE material, and ∇S becomes a non-zero value at the TE-metal interface. The fourth term in Table 3 is the Thomson heat per volume. Essentially, it has the same principle as the Seebeck-Peltier heat because they are all generated due to the change of electrochemical potential during the electrical charge transport process. But to be specified, the Thomson effect allows for the change of Seebeck coefficient for temperature so that it exists inside the TE leg once the Seebeck coefficient is temperature-dependent. The fifth term is the Bridgman's heat. In multi-dimensional cases, if the electrical current density depends on the position, then the term $\nabla \boldsymbol{J}_e$ is no more zero. This contributes to a heat release due to the nonuniform current distribution, which is named as Bridgman effect [173]. However, this term is usually ignored in most of the literature because it only exists when the Seebeck coefficient is anisotropic [172]. The last term in Table 3 is the surface heat loss, which is determined by the temperature difference between TE leg and the surrounding, as well as the effective heat transfer coefficient, including mechanisms of convection and radiation. Then the general heat equation can be written as

$$\dot{q}_{st} = \dot{q}_F + \dot{q}_J + \dot{q}_p + \dot{q}_T + \dot{q}_B + \dot{q}_{loss} \tag{5.19}$$

After considering the detailed expression for each term, ignoring the Bridgman effect, and treating the Peltier heat as a surface heat source, the commonly used governing equation for heat transfer in the isotropic TE element becomes

$$\rho C_p \frac{\partial T}{\partial t} = \nabla(\kappa_{tot} \nabla T) + \frac{\boldsymbol{J}_e^2}{\sigma} - \tau \boldsymbol{J}_e \cdot \nabla T - h_{eff}(T - T_\infty) A_{surface} \ / V \tag{5.20}$$

where $\kappa_{tot} = \kappa_e + \kappa_{lat}$ and h_{eff} is the effective heat transfer coefficient considering both convection and radiation? The simplified version of Eq. (5.19) only includes the term of heat storage at the left side, and the first term of heat conduction, and the second term of Joule heating at the right side. At the steady-state condition, the term in the left-hand side, $\rho C_p \frac{\partial T}{\partial t}$, is set to be zero. Hence, heat storage is necessary to include when there has transient reactions or operating conditions, or the heat capacity of the material is very large. In Eq. (5.20), the third term on the right-hand side is the heat flux due to the Thomson effect, and the fourth term is the heat flux due to convective and radiant heat loss from the TE surface to the surrounding. These two terms can be ignored in some cases, as described before. This heat equation is applicable to both TEG and TEC because it does not include the Seebeck-Peltier heating and cooling explicitly inside the TE leg (excluding the Thomson effect, which can be described as continuous Seebeck effect). The Seebeck-Peltier heating and cooling is only considered at the interface of the TE leg and metal contact, which is written in the boundary conditions. There are different types of boundary conditions for the TE leg under different operating conditions, as listed in Table 4. It showed that different boundary conditions have a significant impact on the energy output of a TEG [174].

Table 4
Boundary conditions.

Module	Side	Boundary conditions
TEC	Hot/cold side surface	$-\kappa\frac{\partial T}{\partial x} = q_{h/c} = h_{h/c}(T - T_\infty)$
	Exterior surface	$-\kappa\frac{\partial T}{\partial y} = h_{eff}(T - T_\infty)$
	Hot side TE-metal interface	$SJ_eT_h - \kappa_{TE}\frac{\partial T_{TE}}{\partial x} + \kappa_{con}\frac{\partial T_{con}}{\partial x} = 0$
	Cold side TE-metal interface	$-SJ_eT_c - \kappa_{TE}\frac{\partial T_{TE}}{\partial x} + \kappa_{con}\frac{\partial T_{con}}{\partial x} = 0$
TEG	Hot/cold side surface	$-\kappa\frac{\partial T}{\partial x} = q_{h/c} = h_{h/c}(T - T_\infty)$
	Exterior surface	$-\kappa\frac{\partial T}{\partial y} = h_{eff}(T - T_\infty)$
	Hot side TE-metal interface	$-SJ_eT_h - \kappa_{TE}\frac{\partial T_{TE}}{\partial x} + \kappa_{con}\frac{\partial T_{con}}{\partial x} = 0$
	Cold side TE-metal interface	$SJ_eT_c - \kappa_{TE}\frac{\partial T_{TE}}{\partial x} + \kappa_{con}\frac{\partial T_{con}}{\partial x} = 0$

Table 3
Volumetric source terms [172].

Fourier ($\dot{q}_F$)	Joule ($\dot{q}_J$)	Peltier ($\dot{q}_P$)	Thomson ($\dot{q}_T$)	Bridgeman ($\dot{q}_B$)	Surface Loss ($\dot{q}_{loss}$)
$\nabla(\kappa_{tot}\nabla T)$	$\boldsymbol{J}_e^2/\sigma$	$\nabla S \cdot \boldsymbol{J}_e T$	$-\tau \boldsymbol{J}_e \cdot \nabla T$	$S \cdot \nabla \boldsymbol{J}_e \cdot T$	$-h_{eff}(T - T_\infty)A_{surface}/V$

The thermoelectric model is a conjugate problem of temperature (T) and electrical current density ($\boldsymbol{J}_e$). Hence, two governing equations are needed for these two unknown fields. The first governing equation is the heat equation, as shown in Section 5.5.1. The other is obtained from the electric equation, as discussed below. The combination of the thermal and electrical models also exists several approaches, including steady-state temperature and electric current based models and transient temperature and electric current based models.

The current density, as shown in Eq. (5.20), depends on both the temperature and the electrostatic potential. This dependence is seen by considering again the BTE, which can be re-written as

$$\boldsymbol{J}_e = -\sigma\nabla\phi - S\sigma\nabla T \tag{5.21}$$

where ϕ is the electrostatic potential ($\boldsymbol{E} = -\nabla\phi$). Eq. (5.21) gives the current densities for the electric current in the medium. The continuity equation of electric charge transport can be used as the electric model:

$$\frac{\partial\rho_{el}}{\partial t} + \nabla\boldsymbol{J}_e = 0 \tag{5.22}$$

In the limit of static carrier distribution, $\frac{\partial\rho_{el}}{\partial t} = 0$, the electrostatic potential can be obtained from the continuity equation where $\nabla\boldsymbol{J}_e = 0$. Then Eq. (5.21) is re-written as

$$\nabla(\sigma\nabla\phi) + \nabla(S\sigma\nabla T) = 0 \tag{5.23}$$

Eqs. (5.20), (5.21) and (5.22) or 5.23 must be solved simultaneously along with the appropriate boundary conditions to obtain the temperature and electrostatic potential distributions across the TEM.

To obtain the transient electrical current density, the electric equation for time need to be considered:

$$\frac{\partial\rho_{el}}{\partial t} + \nabla\boldsymbol{J}_e = 0 \tag{5.24}$$

5.5.2. The full solution of the TE equations

Several researchers have attempted to predict the behavior of TEM using analytical methods, which typically offer the highest accuracy for the lowest computational cost [175–180]. However, to obtain an analytic solution for a complicated PDE, it is necessary to simplify the model, with the temperature dependence of material properties and Thomson effect generally being ignored [181–184]. Efforts are being made to improve the models with the inclusion of these effects [44, 185–188] and the temperature dependence of the material properties [189–191] as well as the heat loss due to convection [170]. Along with considering steady-state heat transfer, transient behavior has also been investigated using different methods to solve the PDEs [180,185,192, 193]. The simplified model has been largely used due to lower computational cost, simplicity, and ease of inclusion into other models. However, analytical methods have inherent limitations due to the inability to consider complex processes and material characteristics. Therefore, its accuracy is limited. To improve the controllability of TEM-based systems, the simplified TEC/TEG models have also been added into the block libraries in SIMULINK/MATLAB as steady-state [194–196] or transient flow charts [195]. So far, due to the complexity of performing 3D transient analysis of TEM, a large number of modeling and control simulations in SIMULINK were based on 1D steady-state governing equations. In addition, the SPICE (Simulation Program with Integrated Circuit Emphasis) software has been used to establish the equivalent circuit model of TEMs using the electric-thermal analogy [197–202]. The SPICE approximation is more accurate for electrical analysis of the system, but the thermal contribution can also be simulated at the same time.

To go beyond simple models, the numerical solution of the PDEs in required. Established methods to solve the governing PDEs include the finite difference method (FDM), the finite volume method (FVM), and the finite element method (FEM), all of which are implemented in a number of commercial and open-source software packages. The difference between these methods lies in how the PDE is discretized. These numerical methods are attractive for simulating TEM performance as the Thomson effect and temperature dependence of materials can be easily included in the governing equations. 1D steady-state [203,204] and 2D transient [205] FDM models were developed and then validated against experimental results, showing a good agreement. A 1D transient model of a TEM solved with FVM [206] also exhibited a good correlation with both experiments and numerical results obtained using the FEM commercial software COMSOL Multiphysics. Another 2D transient model considered the effect of air caves in the 1D model, but it is simpler than the 3D model and easier to combine with other multi-physics models using home-made codes instead of commercial software. The FVM was used to solve the governing equations of the model [207,208] and later using OpenFOAM [209] and FLUENT [210].

The FEM is a more complex approach but with improved accuracy and continuity for models with complex geometry. Most multi-physics simulation software uses the FEM to solve PDEs [211–218] with commercial examples such as ANSYS and COMSOL Multiphysics being the two most widely used. In 2004, El-Genk et al. [11] presented a detailed algorithm for a 3D TEG model based on FEM. Later, in 2005, Antonova and Looman [211] analyzed a TE process using ANSYS. A 3D model was presented in COMSOL Multiphysics and validated against experimental device performance in 2009 [213,216]. Hu et al. [219] investigated the different operating conditions of TEG using COMSOL Multiphysics. In 2015, Wu et al. [220] developed a comprehensive model in COMSOL Multiphysics that considered the influence of chemical potential and carrier density changes. Abaqus FEA is another commercial FEM package that has been used to predict TEM performance [221–228] and with which Richter et al. [183,229] established a transient model for TEM-based heat exchanger. Other models were developed using components from the library TIL in Modelica language. Later, in 2012, Felgner et al. [230] built a TE device simulation model in 2012 using Modelica. The transient behavior and temperature-related TE properties were included. In 2014, Felgner et al. [231] further refined the model and verified it experimentally. As the standard library of Modelica components, the above modules were applied to system simulation in 2014 [232]. The system is an electronic thermostat that uses TEM to recover waste heat from exchangers. In a given simulation scenario, the electricity generated is sufficient to cover the energy consumption of the electronic thermostatic valve. Additionally, some simulations of small TE systems were also reported [233–235].

5.6. Summary and future directions in modeling

Due to the heterogeneous nature of cementitious materials, their measured TE properties (σ, $\kappa = \kappa_{e+}\kappa_{lat}$, S) depend on the formulation, the method of preparation, and the history of the sample. It is important to develop models for calculating TE properties from those of the individual phases, e.g., C–S–H, additives, water, etc. This requires: (1) to calculate these properties for individual components (Sections 5.1-5.3), and (2) models to combine these properties (Sections 5.4-5.6). Here, the successes and limitations and suggestions of future research directions are summarized.

- First-principles calculations based on DFT are feasible for systems with a relatively small unit cell, up to a few hundred atoms. For such systems, they produce very accurate electronic bands and densities of states that serve as the inputs to the BTE to calculate the electronic TE coefficients, i.e. σ, κ_e, and *S*. DFT calculated values compare very well with experimentally measured ones for a wide variety of materials. So far, this has not been applied to cementitious materials, but it has been used successfully for oxides, so it is expected that this works for cement phases as well.
- Lattice thermal conductivities are, to first order, independent of electronic properties. They can be calculated either by *ab initio* methods combined with the phonon BTE or via MD simulations using classical force fields. Both approaches produce values in good agreement with each other and with available experimental data. Given the disordered and porous nature of cementitious materials, it is unclear whether much could be gained by attempting to decrease κ_{lat} further.
- Since first-principles and MD approaches are not practical for meso and macroscopic systems, one has to resort to continuum, analytical or numerical, models. Amongst analytical models, EMT is a very simple option that requires only the relative fraction of each component as input and is reasonably accurate in simple situations. However, it does not take into account the shape, orientation, size, and spatial distribution of the particles. GEMT improves over EMT by incorporating two empirical fitting parameters, which limits its predictive power. A predictive analytical model that takes into account the microscopic morphology in better detail is presently missing. A further challenge is the integration and validation of EMT/GEMT models of the composite transport coefficients into the macroscopic system of partial differential equations described in Section 5.5.1.3.
- While analytical models provide an invaluable qualitative inside, they fail to be predictive if the geometry of the TE devices becomes complicated, e.g., it presents several surfaces, realistic boundary conditions, and no symmetries. The potentiality of finite element modeling (FEM) has been demonstrated for such complicated geometries, but there is only a very limited number of studies of TE composite materials, including cementitious materials. FEM modeling of thermoelectric cementitious materials is still a largely unexplored, worthwhile area of research.
- An aspect that can be very important is to account for the variability of TE parameters, especially the conductance, due to the moisture content. To this end, the established set of partial differential equations must be extended to include the ionic conduction mediated by the adsorbed water. This is especially relevant for cementitious and, in general, porous materials (see Section 3.4), and it is a largely unexplored area of research.
- For the macroscale model development, it is found that the 1-D TEM model has been largely used in analyzing power or heat generation due to its simplicity. It is always considered for system-level due to its computational efficiency. However, the 1-D model lacks accuracy due to the many necessary assumptions. 3-D TEM models have been widely developed in commercially available software and solved by the FEM to obtain better accuracy. However, more complex 3-D models suffer from the high computational expense and, as a result, analytical solutions continue to be of interest for optimization and control studies.
- For the proposed application in buildings, a low-computational-cost and accurate macroscale model that can predict the annual energy consumption for TE envelope, by considering building geometry and locations, annual weather and climate data, ect., will be favored for assessing module and system-level design, operation and control. The life-cycle assessment and life-cycle cost analysis for TE-building envelop system is also necessary to gain to the impact on the environment and design the system more cost-effectively.

6. Conclusions and future research directions

The harvesting of waste heat within the built environment and later reuse of the garnered energy is of high significance in the sustainable energy agenda. The reuse can be for a variety of purposes, such as reducing the load in air conditioning or powering small appliances. It is then not surprising that this topic received considerable attention over the years, hand in hand with improvements in the efficiency of thermoelectric materials. Usually, waste heat harvesting in buildings is achieved by embedding commercial TEG in the walls. However, during the past two decades, there was a consistent effort aiming at developing cementitious materials with good TE properties by exploring a variety of additives. This review examines the experimental research on TE cement composites since 1998, including the fabrication, characterization, composition, and corresponding TE performance. Since TE cement is still at an early stage of research, theoretical models to guide the selection of additive materials are not yet available. Therefore, modeling methods useful to predict the TE properties of individual components and cement composites have also been critically reviewed. Here we summarize the most relevant conclusions of this survey.

TE cement composites exhibit limited electrical conductivity due to the insulating character of the material, thus reducing the figure of merit to impractical levels. Changing the fabrication method from wet to dry mixing and compression is a way to overcome this limitation while eliminating the use of chemical additives. However, a direct comparison between the two methods for the same composition and external conditions is lacking. This comparison is needed to clarify which fabrication method leads to better properties. A more effective way to increase σ has been to mix the cement with materials with high electrical conductivities such as C-based materials, particularly graphene and expanded graphite. Increased electrical conductivity generally implies a lower Seebeck coefficient. The two properties are in competition as *ZT* is proportional to $S^2\sigma$. The Seebeck coefficient of cement is not low, and it can be further improved by mixing with other TE materials, typically oxides, but also Bi_2Te_3 that is an optimal TEM at room temperature. The present trend, and a promising avenue for investigation, is to combine both types of additives, e.g., graphene and oxide nanoparticles, e.g., ZnO. A largely unexplored possibility is the direct doping of the cement, e.g., replacing Si or Ca with non-isovalent species to introduce free carriers. A further enhancement of *ZT* can be achieved by lowering the lattice thermal conductivity. Being cement composites disordered inhomogeneous materials, heat transport via lattice vibrations is already low. In fact, electronic and lattice thermal conductivities are of the same order, so it seems that not much can be gained by further lowering κ_{lat}.

Typically, *ZT* is obtained by measuring the three TE properties (σ, κ, *S*) independently, using different samples and sample geometries, while the measurements are carried out under different operating conditions. It would be desirable to measure the three properties in a single device and, almost simultaneously, to control all possible variables and increase both accuracy and repeatability.

At present, there is no established theory to guide the design of TE cement composites. In particular, it is necessary to determine TE

properties for individual components, e.g., C–S–H and additives, and to develop models that mix them to obtain the properties of composites. First-principles methods combined with the Boltzmann transport equation accomplish the first task with excellent accuracy, but they have never been used to study cement components. Hence an opportunity for research in this direction allows assessing the effect of direct doping of the material. Moving towards mesoscopic or macroscopic samples requires the use of mixing models. The effective medium theory and its generalized version consider the multi-component sample as a homogeneous mixture. Modeling the inhomogeneities and microscopic details due to the size, shape, and orientation distribution of additive particles can be achieved using numerical approaches based on the FEM. There is also scope to improve the analytical models beyond EMT and GEMT, either by theoretical considerations or by using machine learning tools trained on the results of FEM simulations. For the macroscale model development, a 1D simplified analytical model helps to conduct multi-objective optimization and system evaluation quickly. In contrast, the 3-D FEM models in commercial software can present accurate results but are time-consuming. With the proposed application to buildings, an accurate macroscale model at a low computational cost that can predict the annual energy consumption of the TE envelope will be favored for the module and system-level design and operation for TE cement.

Declaration of competing interest

The authors declare that they have no known competing financial interests or personal relationships that could have appeared to influence the work reported in this paper.

Acknowledgments

This research is supported through a US-Ireland grant tri-funded by the National Science Foundation (NSF, 1805818), Science Foundation Ireland (SFI, 17/US/3424), and the Department for the Economy of Northern Ireland (DfE, USI 127).

Appendix

Fundamentals of the thermoelectric phenomenon

When considering the fundamentals of TE materials, an understanding of solid-state physics is required. TE materials can be classified as *n*- and *p*-type according to whether electrons (*n*-type) or holes (*p*-type) are the majority charge carrier responsible for TE effects [236]. Different materials have different Fermi energies, but when a TE material comes into contact with two metallic electrodes, their Fermi energies equalize. Under this circumstance, there is no electrical current through the device, as electrons are in equilibrium. The two main ingredients contributing to electronic conduction are the difference in Fermi distributions between the two contacts and the electronic density of states of the TE material in the region around the Fermi energy. The Fermi distribution difference is zero in equilibrium. Still, it can be modified by imposing a temperature difference (in the Seebeck effect) or a potential difference (in the Peltier effect) between two contacts. In this section, the Landauer-Datta-Lundstrom model is used [117, 237,238] to provide a unique angle of view explaining the physical origins of Seebeck and Peltier effects in detail.

The physical origin of the Seebeck effect

Consider an *n*-type TE material with each of its two ends connected to metal contacts at two temperatures (Fig. A1(a)). The system is in equilibrium as $T_1 = T_2$. When $T_1 > T_2$, the temperature difference starts to drive electrons to move from left to right (Fig. A1(b)). It is because the wider Fermi-Dirac distribution in the hot material (f_1, Fig. A1(c)) implies a finite probability of conduction band states being populated. At the cold end, the distribution is sharper (f_2, Fig. A1(c)). Therefore, the difference between the two Fermi-Dirac distributions is positive when the energy is above the Fermi-level and vice versa (Fig. A1(c)). The consequence is there will be a gradient of electrons states, with a higher density at the hot side and a lower density at the cold side. Electrons then diffuse from the hot end towards the cold end, driven by the electrostatic potential gradient, and will generate a current. In a *p*-type material, it is the holes (imaging electrons move in the opposite direction) that build up at the hot end, leading to the inverse voltage gradient, as shown in Fig. A1(d-f). The Seebeck coefficient, obtained when the current equals zero in an open circuit ($I_e = 0$) is defined as the ratio of the negative voltage gradient to the temperature gradient. Thus, S is negative for *n*-type and positive of *p*-type TE materials.

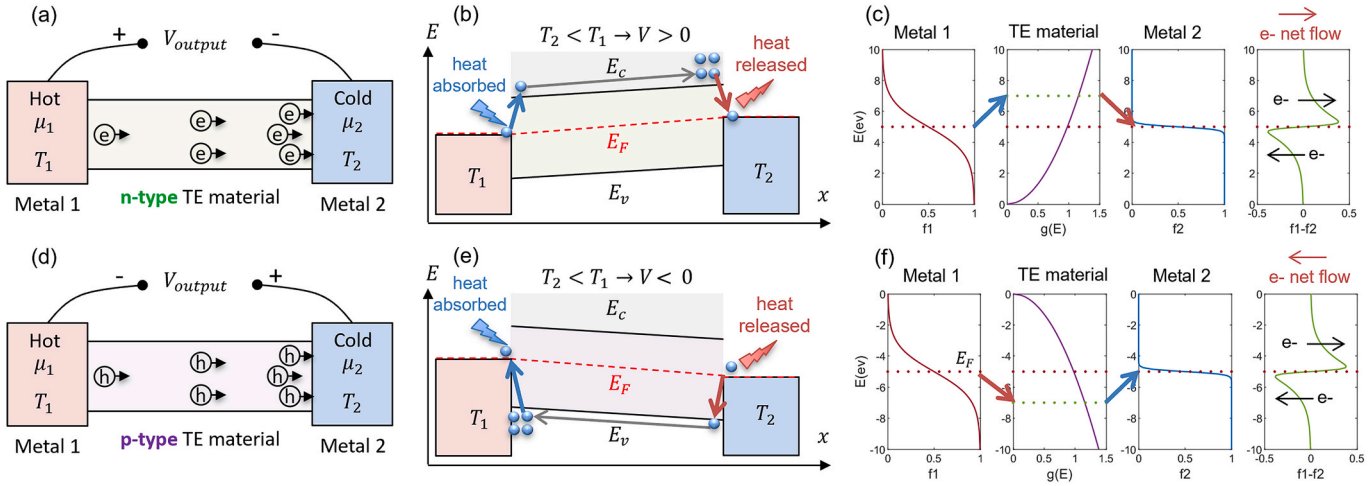

Fig. A1. The energy conversion during electron movement in a TE-Metal system under the generation mode: (a) the schematic diagram, (b) the electron movement and corresponding heat conversion, and (c) the diagrams of Fermi statistic distributions and conductance [$g(E)$] for an *n*-type TE-Metal system; (d) the schematic diagram, (e) the simplified band structure, and (f) the diagrams of Fermi statistic distributions and conductance for a *p*-type TE-Metal system (revised by referring

to Ref. [237]).

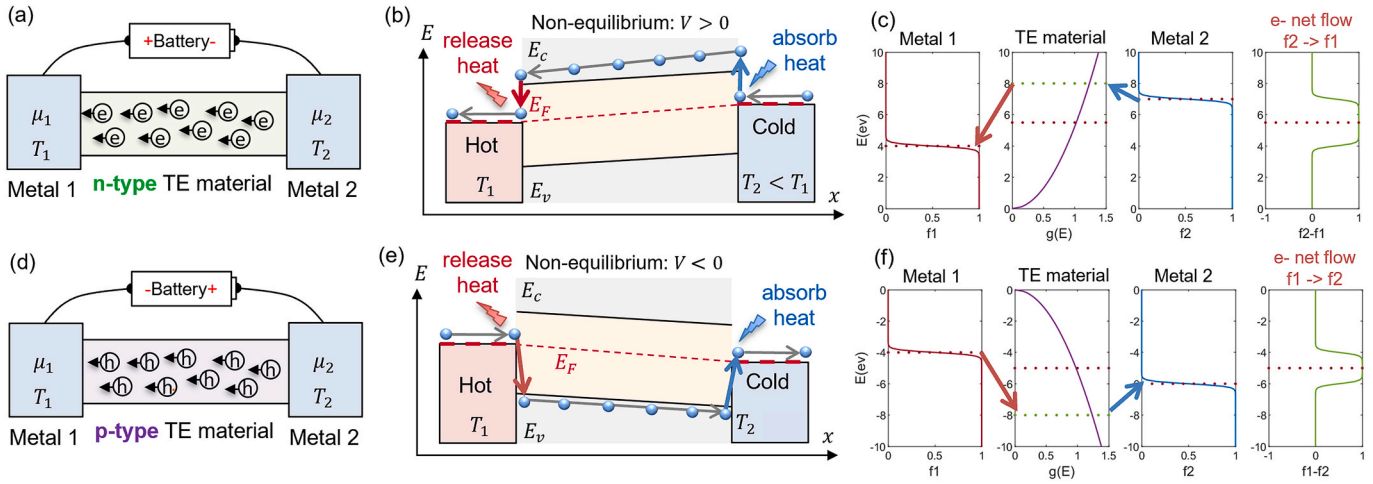

Fig. A2. The energy conversion during electron movement in a TE-Metal system under the cooling mode: (a) the schematic diagram, (b) the electron movement and corresponding heat conversion, and (c) the diagrams of Fermi statistic distributions and conductance for an *n*-type TE-Metal system; (d) the schematic diagram, (e) the simplified band structure, and (f) the diagrams of Fermi statistic distributions and conductance for a *p*-type TE-Metal system (revised by referring to Ref. [237]).

The physical origin of the Peltier effect

Next, the *n*-type TE element in a sandwich-structured module is externally connected to a battery that continually supplies energy (Fig. A2(a)). Initially, the battery is off, and the system is in equilibrium. When the battery is on, the potential of the metal connected to the negative electrode at the right side increases. Hence, a difference in the Fermi-Dirac distribution between the two contacts created (Fig. A2(c)) and electrons flow towards the lower potential. However, an electron needs to absorb energy (in the form of heat), so it can transit to the Fermi window near the conduction band of the TE material and then release it when transiting to Metal 1 (Fig. A2(b-c)). It is the physical origin of the Peltier heating and cooling effect. For a *p*-type material, the movement of holes can be regarded as the opposite movement of electrons, and hence electrons move from Metal 1 to Metal 2 (Fig. A2(d)). They release and absorb heat at the left and right contact, respectively, and Peltier heating and cooling are observed (Fig. A2(d-f)). In this model, the Seebeck coefficient and the Peltier coefficient Π depend on the band structure of the TE material and temperature. The Kelvin equation describes the relationship between Seebeck and Peltier coefficients:

$$\Pi = TS \tag{0.1}$$

Thomson effect

The Seebeck coefficient S is not always independent of temperature. Therefore, for some materials, a temperature gradient can lead to a sizeable gradient of S. This phenomenon was discovered by William Thomson (Lord Kelvin) in 1851 [239]. This gradient of S drives the current so that the Thomson effect could be treated as continuous Peltier effects along with each section of the TE material under different temperature [240]. What determines the direction of the Thomson energy is whether the carriers need to climb or drop to a higher or lower energy level, respectively. So, if S decreases with temperature, the heat will be released in the *n*-type TE material and absorbed in the *p*-type TE material when heat flow and current flow (opposite to electron flow) are in the same direction. Conversely, heat will be absorbed in the *n*-type and released in the *p*-type TE material when heat flow and current flow are in opposite directions. The definition of the Thomson coefficient (the second Kelvin relation) is:

$$\tau = T\, dS/dT$$

Thermoelectric properties

Figure of merit

The overall performance of a TE material or TE device is usually evaluated by a dimensionless indicator ZT, often called the figure of merit:

$$ZT = S^2\sigma\, T/\kappa$$

where σ is the electrical conductivity, and κ is the thermal conductivity. ZT is the guiding quantity for evaluating and optimizing the performance of both TEC and TEG. Current TE materials have $ZT \sim 1$, resulting in the energy-conversion efficiency around 10% at room temperature. In practice, $ZT \geq 3$ is required for a TE material to be competitive with traditional refrigerators and power generators [241,242]. From a device point of view, TE materials should have a large Seebeck coefficient, high electrical conductivity, and low thermal conductivity.

Seebeck coefficient

The Seebeck coefficient or thermopower is an intrinsic material property. The Seebeck coefficient can be conceptually defined in many ways. The

two most common ones are:

(a) as the differential of voltage concerning temperature in a material [6], and
(b) as the entropy per carrier or the ratio of the heat per carrier to temperature [243].

The first one is the most useful definition to determine S experimentally. Typically, thermopowers of metals are of the order of 1–10 μV/K, [243]. For doped semiconductors, the thermopower is of the order 100–1000 μV/K [244]. From the kinetic viewpoint, the Seebeck coefficient yields information about the sign of the charge carriers, the characteristic energy associated with carriers, and the Fermi energy. In metals or degenerate semiconductors, the Seebeck coefficient is better described by Mott's formula [245]:

$$S = \frac{\pi^2}{3}\frac{{k_B}^2 T}{e}\left\{\frac{1}{\sigma(E)}\frac{\mathrm{d}\sigma(E)}{dE}\right\}_{E=E_F} = \frac{\pi^2}{3}\frac{{k_B}^2 T}{e}\left\{\frac{1}{n}\frac{\mathrm{dn}(E)}{dE}+\frac{1}{\mu}\frac{d\mu(E)}{dE}\right\}_{E=E_F}$$

where k_B is Boltzmann's constant, e is the electron charge, and E_F is the Fermi energy. $\sigma(E)$, $n(E)$, $g(E)$, $f(E)$, and $\mu(E)$ represent the electrical conductivity, charge carrier concentration, density of states, Fermi-Dirac function, and mobility as a function of energy, respectively. Notice that these quantities and their derivatives are eventually evaluated at the Fermi energy (E_F), as only chargers within a relatively narrow energy window around E_F participate in conduction phenomena. In the free electron model, $\sigma^{'}/\sigma(E_F) \approx 1/k_B T_F$, is typically small because $T_F \approx 10^4 - 10^5$ K, thus explaining the low thermopower values found in metals. The optimal situation (e.g., a heavily doped semiconductor) should have the Fermi energy (E_F) in a region where the bandgap is on the order of $k_B T$, where T is the desired operating temperature [242,243,246,247]. Generally, a large Seebeck coefficient can be achieved by decreasing the carrier concentration but being careful to maintain a reasonably large electrical conductivity. Tritt et al. [247] suggested that the typical S for best TE performance is within 150–200 μV/K.

Electrical conductivity

The electrical conductivity of a TE material can be regarded as the product of charge density ne and mobility μ:

$$\sigma = ne\mu = ne^2\tau/m^*$$

where τ is the energy-independent relaxation time and m^* is the effective mass of the carrier. Both carrier mobility and concentration vary as a function of temperature and are obtained experimentally from the Hall coefficient and resistivity [248]. In a semiconductor, the temperature-dependent conductivity can be expressed in the Arrhenius form:

$$\sigma = \sigma_0 exp\left(-\frac{\Delta E}{2k_B T}\right)$$

where ΔE is the bandgap energy and σ_0 is a constant. It assumes that the contributing electrons are in a parabolic band with the same density, and the relaxation time is energy independent. The electrical conductivity increases when the thermal energy $k_B T < \Delta E$ [244]. In the optimal situation of a heavily doped semiconductor material (either metal or semiconductor), ZT is optimal at carrier concentrations of about n $\sim 10^{19}$-10^{21} cm^{-3}, for potential TE materials [101].

Promising approaches to achieve higher ZT

Strategies to improve ZT at specific operating temperatures have followed two main avenues: (a) design approaches on known TE materials to optimize three TE properties, and (b) development of new materials with better TE properties. For the first avenue, the electrical power factor ($PF = S^2\sigma$) needs to be maximized while minimizing the thermal conductivity. Several articles reviewed the enhancement of ZT in recent years [33, 249–253]. For the second avenue, one of a new TE material, TE cement composite, is proposed and discussed in the next sections.

Several approaches to maximizing power factor have been used with success. The first is the concept of unusual band structure [249,250,254,255], arising in materials with complex crystal and electronic structure or with strongly correlated electrons to achieve a sharp increase in the electronic density of states near the Fermi level, which allows for an increase in the thermopower. The second concept, pioneered by Hicks and Dresselhaus [251, 252], uses low-dimensional materials such as 2-D superlattices, 1-D quantum wells, and nanowires that have modified electronic transport properties due to the quantum confinement effect on the electronic carriers. It increases the electronic density near the Fermi level by confining the electrons in one dimension while allowing for phonon scattering from the surface of the wire. Other ideas include energy filtering [256], controlled impurity doping to modify transport properties [257], and alloying [258,259].

Increasing the power factor is challenging because an increase in the Seebeck coefficient comes accompanied by a decrease in electrical conductivity. Therefore, a more promising approach is to reduce the lattice thermal conductivity, which is practically decoupled from electronic properties. The first strategy to minimize the lattice thermal conductivity is based on reducing the phonon MFP utilizing Slack's phonon-glass and electron-crystal (PGEC) concept of semiconductors for new TE materials [260]. It can be achieved by replacing a fraction of one of the original elements in the host material with an isoelectronic impurity or an impurity atom with ±1 electron (n or p-type doping). The impurity atoms, which have different mass and size, are dispersed throughout the unit cell of the material and help to scatter phonons on the atomic length scale while maintaining the electronic structure of the material. By increasing the proportion of impurity atoms, one can arrive at a situation where the MFP is reduced. Another way is to insert rattling atoms into the voids or holes present in an open cage or complex structure. These rattlers will oscillate over a range of frequencies within holes and will scatter phonons, effectively reducing the lattice thermal conductivity. Examples of such complex structures include the skutterudites, clathrates, and zintl phases [33,261,262]. The second strategy is to use the mass fluctuation method [254,261] to achieve higher phonon scattering rates over a broad spectrum of frequencies through the inclusion of vacancies, interstitial atoms, and solid solutions. Examples of materials include the Zn_4Sb_3 and Half-Heusler alloys [33,263]. In a third approach, mixing multiphase composites with nanostructured materials can increase phonon scattering. Due to the scale of grains, a corresponding reduction in the phonon MFP can be achieved by grain boundary scattering [255,264–266].

Nomenclature

Symbol		
A	Area	m^2
C	Concentration	kg/kg
c_p	Heat capacity at constant pressure	J/kgK
C_V	Volumetric heat capacity	J/m^3K
e	Electron volt	eV
E	Energy	J
E_F	Fermi energy	J
f	Fermi-Dirac statistics	-
h	Plank constant	$J{\cdot}s$
h_{eff}	Effective heat transfer coefficient	W/m^2K
I	Current	A
J	Current density	A/m^2
k	Thermal conductivity	W/mK
K	Thermal conductance	W/K
k_B	Boltzmann constant	J/K
L	Lorenz number/length	$W\Omega\ /K^2$
m^*	Effective mass of charge carrier	kg
n	Carrier concentration	$1/m^3$
q	Heat per area per second	W/m^2
Q	Heat per second	W
R	Electrical resistance	Ω
S	Seebeck coefficient	V/K
T	Temperature	K
V	Voltage/Volume	V or m^2
Greek		
Λ	Mean free path	m
σ	Electrical conductivity	S/m
τ	Thomson coefficient	V/K
Π	Peltier coefficient	V
μ	Electrochemical potential	J/mol
v	velocity	m/s
Abbreviation		
AC	Alternating current	
BTE	Boltzmann transport equation	
CFRC	Carbon fiber reinforced concrete	
CNT	Carbon nanotube	
COP	Coefficient of performance	
DFT	Density Functional Theory	
DC	Direct Current	
EMT	Effective Medium Theory	
FDM	Finite difference method	
FEM	Finite element method	
FVM	Finite volume method	
GEMT	Generalized Effective Medium Theory	
PAN	polyacrylonitrile	
SCM	supplementary cementing material	
TE	Thermoelectric	
TEM	Thermoelectric module	
TEC/TEH	Thermoelectric cooler/heat pump	
TEG	Thermoelectric generator	
w/c	Water to cement ratio	

References

[1] Global IEA. Energy & CO2 status report. 2018.
[2] Sawin JL, Rutovitz J, Sverrisson F. Renewables 2018 global status report, ISBN 978-3-9818911-3-3.
[3] Semkov K, Mooney E, Connolly M, Adley C. Efficiency improvement through waste heat reduction. Appl Therm Eng 2014;70:716–22. https://doi.org/10.1016/J.APPLTHERMALENG.2014.05.030.
[4] Lawrence livermore national laboratory. U.S energy flow 2013. https://flowcharts.llnl.gov/content/energy/energy_archive/energy_flow_2013/2013USEnergy.png. [Accessed 31 July 2019].
[5] Velmre E. Thomas johann seebeck. Proc Est Acad Sci Eng 2007;13:276–82.
[6] Rowe DM. CRC handbook of thermoelectrics. CRC Press; 1995. https://doi.org/10.1201/9781420049718.
[7] Nag S, Dhar A, Gupta A. Exhaust heat recovery using thermoelectric generators. A Rev. 2017. https://doi.org/10.1007/978-981-10-7575-9_10.
[8] Shen ZG, Tian LL, Liu X. Automotive exhaust thermoelectric generators: current status, challenges and future prospects. Energy Convers Manag 2019. https://doi.org/10.1016/j.enconman.2019.05.087.
[9] Wang D, Liu Y, Jiang J, Pang W, Lau WM, Mei J. Potential application of a thermoelectric generator in passive cooling system of nuclear power plants. J Electron Mater 2017. https://doi.org/10.1007/s11664-016-5191-0.
[10] Rowe DM. Applications of nuclear-powered thermoelectric generators in space. Appl Energy 1991. https://doi.org/10.1016/0306-2619(91)90020-X.
[11] El-Genk M, Saber H, Caillat T. HIGH EFFICIENCY THERMOELECTRIC RADIOISOTOPE POWER SYSTEMS final report. 2004.
[12] Radioisotope NASA. Ower system n.d. https://rps.nasa.gov/power-and-thermal-systems/power-systems/current/.
[13] Li J-F, Liu W-S, Zhao L-D, Zhou M. High-performance nanostructured thermoelectric materials 2010;2:152–8. https://doi.org/10.1038/asiamat.2010.138.
[14] Liu D, Zhao FY, Yang HX, Tang GF. Thermoelectric mini cooler coupled with micro thermosiphon for CPU cooling system. Energy 2015. https://doi.org/10.1016/j.energy.2015.01.098.
[15] Cheng K, Qin J, Sun H, Dang C, Zhang S, Liu X, et al. Performance assessment of an integrated power generation and refrigeration system on hypersonic vehicles. Aero Sci Technol 2019. https://doi.org/10.1016/j.ast.2019.04.006.
[16] Kishore RA, Nozariasbmarz A, Poudel B, Sanghadasa M, Priya S. Ultra-high performance wearable thermoelectric coolers with less materials. Nat Commun 2019. https://doi.org/10.1038/s41467-019-09707-8.

[17] Hasebe M, Kamikawa Y, Meiarashi S. Thermoelectric generators using solar thermal energy in heated road pavement. 2006 25th int. Conf. Thermoelectr. IEEE; 2006. p. 697–700. https://doi.org/10.1109/ICT.2006.331237.

[18] Tahami SA, Gholikhani M, Nasouri R, Dessouky S, Papagiannakis AT. Developing a new thermoelectric approach for energy harvesting from asphalt pavements. Appl Energy 2019. https://doi.org/10.1016/j.apenergy.2019.01.152.

[19] Datta U, Dessouky S, Papagiannakis AT. Harvesting thermoelectric energy from asphalt pavements. Transp Res Rec J Transp Res Board 2017;2628:12–22. https://doi.org/10.3141/2628-02.

[20] Jiang W, Yuan D, Xu S, Hu H, Xiao J, Sha A, et al. Energy harvesting from asphalt pavement using thermoelectric technology. Appl Energy 2017. https://doi.org/10.1016/j.apenergy.2017.08.091.

[21] Jiang W, Xiao J, Yuan D, Lu H, Xu S, Huang Y. Design and experiment of thermoelectric asphalt pavements with power-generation and temperature-reduction functions. Energy Build 2018. https://doi.org/10.1016/j.enbuild.2018.03.049.

[22] Khire RA, Messac A, Van Dessel S. Design of thermoelectric heat pump unit for active building envelope systems. Int J Heat Mass Tran 2005;48:4028–40. https://doi.org/10.1016/J.IJHEATMASSTRANSFER.2005.04.028.

[23] Liu Z, Zhang L, Gong G, Luo Y, Meng F. Evaluation of a prototype active solar thermoelectric radiant wall system in winter conditions. Appl Therm Eng 2015;89:36–43. https://doi.org/10.1016/J.APPLTHERMALENG.2015.05.076.

[24] Liu Z, Zhang L, Gong G, Han T. Experimental evaluation of an active solar thermoelectric radiant wall system. Energy Convers Manag 2015;94:253–60. https://doi.org/10.1016/J.ENCONMAN.2015.01.077.

[25] Liu ZB, Zhang L, Gong G, Luo Y, Meng F. Experimental study and performance analysis of a solar thermoelectric air conditioner with hot water supply. Energy Build 2015;86:619–25. https://doi.org/10.1016/J.ENBUILD.2014.10.053.

[26] Ibañez-Puy M, Martín-Gómez C, Bermejo-Busto J, Sacristán JA, Ibañez-Puy E. Ventilated active thermoelectric envelope (VATE): analysis of its energy performance when integrated in a building. Energy Build 2018;158:1586–92. https://doi.org/10.1016/J.ENBUILD.2017.11.037.

[27] Irshad K, Habib K, Thirumalaiswamy N, Saha BB. Performance analysis of a thermoelectric air duct system for energy-efficient buildings. Energy 2015;91:1009–17. https://doi.org/10.1016/J.ENERGY.2015.08.102.

[28] He W, Zhou J, Hou J, Chen C, Ji J. Theoretical and experimental investigation on a thermoelectric cooling and heating system driven by solar. Appl Energy 2013;107:89–97. https://doi.org/10.1016/J.APENERGY.2013.01.055.

[29] He W, Zhou J, Chen C, Ji J. Experimental study and performance analysis of a thermoelectric cooling and heating system driven by a photovoltaic/thermal system in summer and winter operation modes. Energy Convers Manag 2014;84:41–9. https://doi.org/10.1016/J.ENCONMAN.2014.04.019.

[30] Chen J, Zhao D, Ge H, Wang J. Graphene oxide-deposited carbon fiber/cement composites for electromagnetic interference shielding application. Construct Build Mater 2015;84:66–72. https://doi.org/10.1016/J.CONBUILDMAT.2015.03.050.

[31] Selvan KV, Hasan MN, Mohamed Ali MS. State-of-the-Art reviews and analyses of emerging research findings and achievements of thermoelectric materials over the past years. J Electron Mater 2019;48:745–77. https://doi.org/10.1007/s11664-018-06838-4.

[32] Zhao D, Tan G. A review of thermoelectric cooling: materials, modeling and applications. Appl Therm Eng 2014. https://doi.org/10.1016/j.applthermaleng.2014.01.074.

[33] Alam H, Ramakrishna S. A review on the enhancement of figure of merit from bulk to nano-thermoelectric materials. Nanomater Energy 2013;2:190–212. https://doi.org/10.1016/j.nanoen.2012.10.005.

[34] Kamarudin MA, Sahamir SR, Datta RS, Long BD, Mohd Sabri MF, Mohd Said S. A review on the fabrication of polymer-based thermoelectric materials and fabrication methods. Sci World J 2013;2013. https://doi.org/10.1155/2013/713640.

[35] Sundarraj P, Maity D, Roy SS, Taylor RA. Recent advances in thermoelectric materials and solar thermoelectric generators-a critical review. RSC Adv 2014;4:46860–74. https://doi.org/10.1039/c4ra05322b.

[36] Gaultois MW, Sparks TD, Borg CKH, Seshadri R, Bonificio WD, Clarke DR. Data-driven review of thermoelectric materials: performance and resource considerations. Chem Mater 2013;25:2911–20. https://doi.org/10.1021/cm400893e.

[37] Cowen LM, Atoyo J, Carnie MJ, Baran D, Schroeder BC. Review-organic materials for thermoelectric energy generation. ECS J Solid State Sci Technol 2017;6:N3080–8. https://doi.org/10.1149/2.0121703jss.

[38] Peng S, Wang D, Lu J, He M, Xu C, Li Y, et al. A review on organic polymer-based thermoelectric materials. J Polym Environ 2017;25:1208–18. https://doi.org/10.1007/s10924-016-0895-z.

[39] Yin Y, Baskaran K, Tiwari A. A review of strategies for developing promising thermoelectric materials by controlling thermal conduction. Phys Status Solidi Appl Mater Sci 2019;1800904:6–8. https://doi.org/10.1002/pssa.201800904.

[40] Selvan KV, Hasan MN, Mohamed Ali MS. Methodological reviews and analyses on the emerging research trends and progresses of thermoelectric generators. Int J Energy Res 2019;43:113–40. https://doi.org/10.1002/er.4206.

[41] Yan J, Liao X, Yan D, Chen Y. Review of micro thermoelectric generator. J Microelectromech Syst 2018;27:1–18. https://doi.org/10.1109/JMEMS.2017.2782748.

[42] Wang H, Chu W, Chen G. A brief review on measuring methods of thermal conductivity of organic and hybrid thermoelectric materials. Adv Electron Mater 2019:1900167. https://doi.org/10.1002/aelm.201900167.

[43] He R, Schierning G, Nielsch K. Thermoelectric devices: a review of devices, architectures, and contact optimization. Adv Mater Technol 2018;3. https://doi.org/10.1002/admt.201700256.

[44] Twaha S, Zhu J, Yan Y, Li B. A comprehensive review of thermoelectric technology: materials, applications, modelling and performance improvement. Renew Sustain Energy Rev 2016;65:698–726. https://doi.org/10.1016/j.rser.2016.07.034.

[45] Ding LC, Akbarzadeh A, Tan L. A review of power generation with thermoelectric system and its alternative with solar ponds. Renew Sustain Energy Rev 2018;81:799–812. https://doi.org/10.1016/j.rser.2017.08.010.

[46] Ando Junior OH, Maran ALO, Henao NC. A review of the development and applications of thermoelectric microgenerators for energy harvesting. Renew Sustain Energy Rev 2018;91:376–93. https://doi.org/10.1016/j.rser.2018.03.052.

[47] Alghoul MA, Shahahmadi SA, Yeganeh B, Asim N, Elbreki AM, Sopian K, et al. A review of thermoelectric power generation systems: roles of existing test rigs/prototypes and their associated cooling units on output performance. Energy Convers Manag 2018;174:138–56. https://doi.org/10.1016/j.enconman.2018.08.019.

[48] Karthick K, Suresh S, Hussain MMMD, Ali HM, Kumar CSS. Evaluation of solar thermal system configurations for thermoelectric generator applications: a critical review. Sol Energy 2019;188:111–42. https://doi.org/10.1016/j.solener.2019.05.075.

[49] Sarbu I, Dorca A. A comprehensive review of solar thermoelectric cooling systems. Int J Energy Res 2018;42:395–415. https://doi.org/10.1002/er.3795.

[50] Irshad K, Habib K, Saidur R, Kareem MW, Saha BB. Study of thermoelectric and photovoltaic facade system for energy efficient building development: a review. J Clean Prod 2019;209:1376–95. https://doi.org/10.1016/J.JCLEPRO.2018.09.245.

[51] Babu C, Ponnambalam P. The role of thermoelectric generators in the hybrid PV/T systems: a review. Energy Convers Manag 2017;151:368–85. https://doi.org/10.1016/j.enconman.2017.08.060.

[52] Champier D. Thermoelectric generators: a review of applications. Energy Convers Manag 2017;140:167–81. https://doi.org/10.1016/J.ENCONMAN.2017.02.070.

[53] Patil DS, Arakerimath RR, Walke PV. Thermoelectric materials and heat exchangers for power generation – a review. Renew Sustain Energy Rev 2018;95:1–22. https://doi.org/10.1016/j.rser.2018.07.003.

[54] ASTM International. C192/C192M-19 standard practice for making and curing concrete test specimens in the laboratory. ASTM Int; 2019. https://doi.org/10.1520/C0192_C0192M-19. . [Accessed 6 July 2020].

[55] ASTM international. C31/C31M − 19a standard practice for making and curing concrete test specimens in the field 1. ASTM Int 2019. https://doi.org/10.1520/C0031_C0031M-19A.

[56] Wei J, Zhang Q, Zhao L, Hao L, Nie Z. Effect of moisture on the thermoelectric properties in expanded graphite/carbon fiber cement composites. Ceram Int 2017;43:10763–9. https://doi.org/10.1016/J.CERAMINT.2017.05.088.

[57] Wei J, Zhao L, Zhang Q, Nie Z, Hao L. Enhanced thermoelectric properties of cement-based composites with expanded graphite for climate adaptation and large-scale energy harvesting. Energy Build 2018;159:66–74. https://doi.org/10.1016/J.ENBUILD.2017.10.032.

[58] Wei J, Fan Y, Zhao L, Xue F, Hao L, Zhang Q. Thermoelectric properties of carbon nanotube reinforced cement-based composites fabricated by compression shear. Ceram Int 2018;44:5829–33. https://doi.org/10.1016/J.CERAMINT.2018.01.074.

[59] Ghosh S, Harish S, Rocky KA, Ohtaki M, Saha BB. Graphene enhanced thermoelectric properties of cement based composites for building energy harvesting. Energy Build 2019:109419. https://doi.org/10.1016/j.enbuild.2019.109419.

[60] Ghosh S, Harish S, Ohtaki M, Saha BB. Enhanced figure of merit of cement composites with graphene and ZnO nanoinclusions for efficient energy harvesting in buildings. Energy 2020;198:117396. https://doi.org/10.1016/j.energy.2020.117396.

[61] Heaney MichaelB. Electrical conductvity and resistivity, electrical measurement, signal processing, and displays. 2003.

[62] Layssi H, Ghods P, Alizadeh AR, Salehi M. Electrical resistivity of concrete concepts, applications, and measurement techniques. n.d.

[63] Polder RB. Test methods for on site measurement of resistivity of concrete - a RILEM TC-154 technical recommendation. Construct Build Mater 2001;15:125–31. https://doi.org/10.1016/S0950-0618(00)00061-1.

[64] Lataste JF, Sirieix C, Breysse D, Frappa M. Electrical resistivity measurement applied to cracking assessment on reinforced concrete structures in civil engineering. NDT E Int 2003;36:383–94. https://doi.org/10.1016/S0963-8695(03)00013-6.

[65] Ratna D. Thermal properties of thermosets. Thermosets, Elsevier; 2012. p. 62–91. https://doi.org/10.1533/9780857097637.1.62.

[66] Real S, Gomes MG, Moret Rodrigues A, Bogas JA. Contribution of structural lightweight aggregate concrete to the reduction of thermal bridging effect in buildings. Construct Build Mater 2016;121:460–70. https://doi.org/10.1016/j.conbuildmat.2016.06.018.

[67] The One-Dimensional Heat Equation. 23, Cambridge University press; 1984.

[68] Budaiwi I, Abdou ; A, Al-Homoud M. Variations of thermal conductivity of insulation materials under different operating temperatures: impact on envelope-induced cooling load n.d. doi:10.1061/ASCE1076-043120028:4125.

[69] Gomes MG, Flores-Colen I, Manga LM, Soares A, de Brito J. The influence of moisture content on the thermal conductivity of external thermal mortars.

Construct Build Mater 2017;135:279–86. https://doi.org/10.1016/j.conbuildmat.2016.12.166.
[70] Bindiganavile V, Batool F, Suresh N. Effect of fly ash on thermal properties of cement based foams evaluated by transient plane heat source. Indian Concr J 2012;86:7–14.
[71] Asadi I, Shafigh P, Abu Hassan ZF Bin, Mahyuddin NB. Thermal conductivity of concrete – a review. J Build Eng 2018;20:81–93. https://doi.org/10.1016/j.jobe.2018.07.002.
[72] Gandage AS, Rao VRV, Sivakumar MVN, Vasan A, Venu M, Yaswanth AB. Effect of perlite on thermal conductivity of self compacting concrete. Procedia - Soc Behav Sci 2013;104:188–97. https://doi.org/10.1016/j.sbspro.2013.11.111.
[73] Taoukil D, El Bouardi A, Sick F, Mimet A, Ezbakhe H, Ajzoul T. Moisture content influence on the thermal conductivity and diffusivity of wood-concrete composite. Construct Build Mater 2013;48:104–15. https://doi.org/10.1016/j.conbuildmat.2013.06.067.
[74] Yang I, Kim D, Lee S. Construction and preliminary testing of a guarded hot plate apparatus for thermal conductivity measurements at high temperatures. Int J Heat Mass Tran 2018;122:1343–52. https://doi.org/10.1016/j.ijheatmasstransfer.2018.02.072.
[75] Merckx B, Dudoignon P, Garnier JP, Marchand D. Simplified transient hot-wire method for effective thermal conductivity measurement in geo materials: microstructure and saturation effect. Adv Civ Eng 2012;2012. https://doi.org/10.1155/2012/625395.
[76] Rodert HM. A transient hot wire thermal conductivity apparatus for fluids*. vol. vol. 86. n.d.
[77] Healy JJ, de Groot JJ, Kestin J. The theory of the transient hot-wire method for measuring thermal conductivity. Phys B+C 1976;82:392–408. https://doi.org/10.1016/0378-4363(76)90203-5.
[78] Log T, Gustafsson SE. Transient plane source (TPS) technique for measuring thermal transport properties of building materials. Fire Mater 1995;19:43–9. https://doi.org/10.1002/fam.810190107.
[79] Gustafsson SE. Transient plane source techniques for thermal conductivity and thermal diffusivity measurements of solid materials. Rev Sci Instrum 1991;62:797–804. https://doi.org/10.1063/1.1142087.
[80] Santos WN dos, Gregório R. Numerical and experimental determination of the minimum and maximum measuring times for the hot wire parallel technique. Cerâmica 2003;49:29–35. https://doi.org/10.1590/s0366-69132003000100007.
[81] Parker WJ, Jenkins RJ, Butler CP, Abbott GL. Flash method of determining thermal diffusivity, heat capacity, and thermal conductivity. J Appl Phys 1961;32:1679–84. https://doi.org/10.1063/1.1728417.
[82] Yüksel N. The review of some commonly used methods and techniques to measure the thermal conductivity of insulation materials. Insul. Mater. Context sustain. InTech; 2016. https://doi.org/10.5772/64157.
[83] Ogawa M, Mukai K, Fukui T, Baba T. The development of a thermal diffusivity reference material using alumina. Meas Sci Technol 2001;12:2058. https://doi.org/10.1088/0957-0233/12/12/305.
[84] Vozár L, Hohenauer W. Uncertainty of thermal diffusivity measurements using the laser flash method. Int J Thermophys 2005;26:1899–915. https://doi.org/10.1007/s10765-005-8604-5.
[85] Hay B, Filtz JR, Hameury J, Rongione L. Uncertainty of thermal diffusivity measurements by laser flash method. Int J Thermophys 2005;26:1883–98. https://doi.org/10.1007/s10765-005-8603-6.
[86] Sun M, Li Z, Mao Q, Shen D. Thermoelectric percolation phenomena in carbon fiber-reinforced concrete. Cement Concr Res 1998;28:1707–12. https://doi.org/10.1016/S0008-8846(98)00161-6.
[87] Wen S, Chung DD. Seebeck effect in carbon fiber-reinforced cement. Cement Concr Res 1999;29:1989–93. https://doi.org/10.1016/S0008-8846(99)00185-4.
[88] Wen S, Chung DD. Enhancing the Seebeck effect in carbon fiber-reinforced cement by using intercalated carbon fibers. Cement Concr Res 2000;30:1295–8. https://doi.org/10.1016/S0008-8846(00)00341-0.
[89] Bahar D, Salih Y. Thermoelectric behavior of carbon fiber reinforced lightweight concrete with mineral admixtures. N Carbon Mater 2008;23:21–4. https://doi.org/10.1016/S1872-5805(08)60009-8.
[90] Wei J, Nie Z, He G, Hao L, Zhao L, Zhang Q. Energy harvesting from solar irradiation in cities using the thermoelectric behavior of carbon fiber reinforced cement composites. RSC Adv 2014;4:48128–34. https://doi.org/10.1039/C4RA07864K.
[91] Tzounis L, Liebscher M, Fuge R, Leonhardt A, Mechtcherine V. P- and n-type thermoelectric cement composites with CVD grown p- and n-doped carbon nanotubes: demonstration of a structural thermoelectric generator. Energy Build 2019;191:151–63. https://doi.org/10.1016/j.enbuild.2019.03.027.
[92] Wen S, Chung DD. Seebeck effect in steel fiber reinforced cement. Cement Concr Res 2000;30:661–4. https://doi.org/10.1016/S0008-8846(00)00205-2.
[93] Wei J, Hao L, He GP, Yang CL. Thermoelectric power of carbon fiber reinforced cement composites enhanced by Ca3Co4O9. Appl Mech Mater 2013;320:354–7. https://doi.org/10.4028/www.scientific.net/AMM.320.354.
[94] Wei J, Hao L, He G, Yang C. Enhanced thermoelectric effect of carbon fiber reinforced cement composites by metallic oxide/cement interface. Ceram Int 2014;40:8261–3. https://doi.org/10.1016/J.CERAMINT.2014.01.024.
[95] Ji T, Zhang X, Zhang X, Zhang Y, Li W. Effect of manganese dioxide nanorods on the thermoelectric properties of cement composites. J Mater Civ Eng 2018;30:04018224. https://doi.org/10.1061/(ASCE)MT.1943-5533.0002401.
[96] Ghahari S, Ghafari E, Lu N. Effect of ZnO nanoparticles on thermoelectric properties of cement composite for waste heat harvesting. Construct Build Mater 2017;146:755–63. https://doi.org/10.1016/J.CONBUILDMAT.2017.04.165.
[97] Wei J, Zhang Q, Zhao L, Hao L, Yang C. Enhanced thermoelectric properties of carbon fiber reinforced cement composites. Ceram Int 2016;42:11568–73. https://doi.org/10.1016/J.CERAMINT.2016.04.014.
[98] Quantum design North America - products - PPMS® DynaCoolTM – quantum design n.d. https://www.qdusa.com/products/dynacool.html. [Accessed 9 July 2020].
[99] Martin J, Tritt T, Uher C. High temperature Seebeck coefficient metrology. J Appl Phys 2010;108:121101. https://doi.org/10.1063/1.3503505.
[100] Ji T, Zhang X, Li W. Enhanced thermoelectric effect of cement composite by addition of metallic oxide nanopowders for energy harvesting in buildings. Construct Build Mater 2016;115:576–81. https://doi.org/10.1016/j.conbuildmat.2016.04.035.
[101] Snyder GJ, Toberer ES. Complex thermoelectric materials. Nat Mater 2008;7:105–14. https://doi.org/10.1038/nmat2090.
[102] Chen N, Gascoin F, Snyder GJ, Müller E, Karpinski G, Stiewe C. Macroscopic thermoelectric inhomogeneities in (AgSbTe 2) x (PbTe) 1-x. Appl Phys Lett 2005;87:1–3. https://doi.org/10.1063/1.2056590.
[103] Hansson ILH, Hansson CM. Electrical resistivity measurements of Portland cement based materials. Cement Concr Res 1983;13:675–83. https://doi.org/10.1016/0008-8846(83)90057-1.
[104] Armoosh SR, Oltulu M. Effect of different micro metal powders on the electrical resistivity of cementitious composites. IOP Conf Ser Mater Sci Eng 2019;471. https://doi.org/10.1088/1757-899X/471/3/032075.
[105] Xie P, Gu P, Beaudoin JJ. Electrical percolation phenomena in cement composites containing conductive fibres. J Mater Sci 1996;31:4093–7. https://doi.org/10.1007/BF00352673.
[106] Azarsa P, Gupta R. Electrical resistivity of concrete for durability evaluation: a review. Ann Mater Sci Eng 2017;2017:1–30. https://doi.org/10.1155/2017/8453095.
[107] Dong W, Li W, Long G, Tao Z, Li J, Wang K. Electrical resistivity and mechanical properties of cementitious composite incorporating conductive rubber fibres. Smart Mater Struct 2019;28. https://doi.org/10.1088/1361-665X/ab282a.
[108] Gandía-Romero JM, Ramón JE, Bataller R, Palací DG, Valcuende M, Soto J. Influence of the area and distance between electrodes on resistivity measurements of concrete. Mater Struct Constr 2017;50. https://doi.org/10.1617/s11527-016-0925-2.
[109] Shirvanimoghaddam K, Hamim SU, Karbalaei Akbari M, Fakhrhoseini SM, Khayyam H, Pakseresht AH, et al. Carbon fiber reinforced metal matrix composites: fabrication processes and properties. Compos Part A Appl Sci Manuf 2017;92:70–96. https://doi.org/10.1016/J.COMPOSITESA.2016.10.032.
[110] Morgan P. Carbon fibers and their composites, vol. 27. CRC Press; 2005. https://doi.org/10.1201/9781420028744.
[111] Newcomb BA. Carbon fibers. Kirk-othmer encycl. Chem. Technol. Hoboken, NJ, USA: John Wiley & Sons, Inc.; 2017. p. 1–21. https://doi.org/10.1002/0471238961.0301180222051411.a01.pub3.
[112] Newcomb BA. Processing, structure, and properties of carbon fibers. Compos Part A Appl Sci Manuf 2016;91:262–82. https://doi.org/10.1016/J.COMPOSITESA.2016.10.018.
[113] Li A, Ma Z, Song H, Lu K, Liu Z, Guo Q. Effect of heat treatment temperature on the microstructure and properties of polyimide-based carbon fibers. Carbon N Y 2015;85:447. https://doi.org/10.1016/J.CARBON.2014.12.079.
[114] Tunakova V, Gregr J, Šafářová V, Grégr J. Electrical conductivity measurement OF fibers and yarns. Liberec, Czech Republic: 7th Int. Conf. - TEXSCI 2010; 2010.
[115] Sun M, Li Z, Mao Q, Shen D. Study on the hole conduction phenomenon in carbon fiber-reinforced concrete. Cement Concr Res 1998;28:549–54. https://doi.org/10.1016/S0008-8846(98)00011-8.
[116] Gatzen HH, Saile V, Leuthold J. Nanofabrication by self-assembly. Micro nano fabr. Berlin, Heidelberg: Springer Berlin Heidelberg; 2015. p. 409–23. https://doi.org/10.1007/978-3-662-44395-8_8.
[117] Chakraborty P, Ma T, Zahiri AH, Cao L, Wang Y. Carbon-based materials for thermoelectrics. Adv Condens Matter Phys 2018;2018:1–29. https://doi.org/10.1155/2018/3898479.
[118] Blackburn JL, Ferguson AJ, Cho C, Grunlan JC. Carbon-nanotube-based thermoelectric materials and devices. Adv Mater 2018;30:1704386. https://doi.org/10.1002/adma.201704386.
[119] Taherian R, Kausar A, Taherian R. Application of polymer-based composites: bipolar plate of PEM fuel cells. Electr Conduct Polym Compos 2019:183–237. https://doi.org/10.1016/B978-0-12-812541-0.00007-0.
[120] Malik R, Tomer VK, Chaudhary V. Hybridized graphene for chemical sensing. Funct. Graphene nanocomposites their deriv. Elsevier; 2019. p. 323–38. https://doi.org/10.1016/b978-0-12-814548-7.00016-7.
[121] Wen S, Chung DDL. Cement-based thermocouples. Cement Concr Res 2001;31:507–10. https://doi.org/10.1016/S0008-8846(00)00391-4.
[122] Clemens J. M. Lasance. The Seebeck coefficient | electronics cooling n.d. https://www.electronics-cooling.com/2006/11/the-seebeck-coefficient/. [Accessed 3 April 2019].
[123] Rudradawong C, Kitiwan M, Goto T, Ruttanapun C. Positive ionic conduction of mayenite cement Ca12Al14O33/nano-carbon black composites on dielectric and thermoelectric properties. Mater Today Commun 2020;22:100820. https://doi.org/10.1016/j.mtcomm.2019.100820.
[124] Wei J, Wang Y, Li X, Jia Z, Qiao S, Zhang Q, et al. Effect of porosity and crack on the thermoelectric properties of expanded graphite/carbon fiber reinforced cement-based composites. Int J Energy Res 2020;44:6885–93. https://doi.org/10.1002/er.5437.

[125] Wen S, Chung DDDL. Origin of the thermoelectric behavior of steel fiber cement paste. Cement Concr Res 2002;32:821–3. https://doi.org/10.1016/S0008-8846(01)00754-2.

[126] Perdew JP, Burke K, Ernzerhof M. Generalized gradient approximation made simple. Phys Rev Lett 1996;77:3865–8. https://doi.org/10.1103/PhysRevLett.77.3865.

[127] Kohanoff J. Electronic structure calculations for solids and molecules: theory and computational methods, vol. 9780521815918. Cambridge University Press; 2006. https://doi.org/10.1017/CBO9780511755613.

[128] Churakov SV. Hydrogen bond connectivity in jennite from ab initio simulations. Cement Concr Res 2008;38:1359–64. https://doi.org/10.1016/j.cemconres.2008.08.004.

[129] Moon J, Yoon S, Monteiro PJM. Mechanical properties of jennite: a theoretical and experimental study. Cement Concr Res 2015;71:106–14. https://doi.org/10.1016/j.cemconres.2015.02.005.

[130] Churakov SV. Hydrogen bond connectivity in jennite from ab initio simulations. Cement Concr Res 2008;38:1359–64. https://doi.org/10.1016/j.cemconres.2008.08.004.

[131] Dezerald L, Kohanoff JJ, Correa AA, Caro A, Pellenq RJM, Ulm FJ, et al. Cement as a waste form for nuclear fission products: the case of 90Sr and its daughters. Environ Sci Technol 2015;49:13676–83. https://doi.org/10.1021/acs.est.5b02609.

[132] Le Caër S, Dezerald L, Boukari K, Lainé M, Taupin S, Kavanagh RM, et al. Production of H2 by water radiolysis in cement paste under electron irradiation: a joint experimental and theoretical study. Cement Concr Res 2017;100:110–8. https://doi.org/10.1016/j.cemconres.2017.05.022.

[133] Abdolhosseini Qomi MJ, Krakowiak KJ, Bauchy M, Stewart KL, Shahsavari R, Jagannathan D, et al. Combinatorial molecular optimization of cement hydrates. Nat Commun 2014;5:1–10. https://doi.org/10.1038/ncomms5960.

[134] Gartner E, Maruyama I, Chen J. A new model for the C-S-H phase formed during the hydration of Portland cements. Cement Concr Res 2017;97:95–106. https://doi.org/10.1016/j.cemconres.2017.03.001.

[135] Kumar A, Walder BJ, Kunhi Mohamed A, Hofstetter A, Srinivasan B, Rossini AJ, et al. The atomic-level structure of cementitious calcium silicate hydrate. J Phys Chem C 2017;121:17188–96. https://doi.org/10.1021/acs.jpcc.7b02439.

[136] Cygan RT, Liang JJ, Kalinichev AG. Molecular models of hydroxide, oxyhydroxide, and clay phases and the development of a general force field. J Phys Chem B 2004;108:1255–66. https://doi.org/10.1021/jp0363287.

[137] Tavakoli D, Tarighat A. Molecular dynamics study on the mechanical properties of Portland cement clinker phases. Comput Mater Sci 2016;119:65–73. https://doi.org/10.1016/j.commatsci.2016.03.043.

[138] Heinz H, Lin TJ, Kishore Mishra R, Emami FS. Thermodynamically consistent force fields for the assembly of inorganic, organic, and biological nanostructures: the INTERFACE force field. Langmuir 2013;29:1754–65. https://doi.org/10.1021/la3038846.

[139] Shahsavari R, Pellenq RJM, Ulm FJ. Empirical force fields for complex hydrated calcio-silicate layered materials. Phys Chem Chem Phys 2011;13:1002–11. https://doi.org/10.1039/c0cp00516a.

[140] Galmarini S, Kunhi Mohamed A, Bowen P. Atomistic simulations of silicate species interaction with portlandite surfaces. J Phys Chem C 2016;120:22407–13. https://doi.org/10.1021/acs.jpcc.6b07044.

[141] Liu L, Jaramillo-Botero A, Goddard WA, Sun H. Development of a ReaxFF reactive force field for ettringite and study of its mechanical failure modes from reactive dynamics simulations. J Phys Chem 2012;116:3918–25. https://doi.org/10.1021/jp210135j.

[142] Wang T, Zhang C, Snoussi H, Zhang G. Machine learning approaches for thermoelectric materials research. Adv Funct Mater 2020;30:1906041. https://doi.org/10.1002/adfm.201906041.

[143] Uher C. Thermal conductivity of metals. Therm. Conduct. Springer US; 2006. p. 21–91. https://doi.org/10.1007/0-387-26017-x_2.

[144] Madsen GKH, Singh DJ. BoltzTraP. A code for calculating band-structure dependent quantities. 2006. https://doi.org/10.1016/j.cpc.2006.03.007.

[145] Lo S-H, He J, Biswas K, Kanatzidis MG, Dravid VP. Phonon scattering and thermal conductivity in p-type nanostructured PbTe-BaTe bulk thermoelectric materials. Adv Funct Mater 2012;22:5175–84. https://doi.org/10.1002/adfm.201201221.

[146] Madsen GKH, Singh DJ. BoltzTraP. A code for calculating band-structure dependent quantities. Comput Phys Commun 2006;175:67–71. https://doi.org/10.1016/j.cpc.2006.03.007.

[147] Madsen GKH, Carrete J, Verstraete MJ. BoltzTraP2, a program for interpolating band structures and calculating semi-classical transport coefficients. Comput Phys Commun 2018;231:140–5. https://doi.org/10.1016/j.cpc.2018.05.010.

[148] Bilc DI, Floare CG, Zârbo LP, Garabagiu S, Lemal S, Ghosez P. First-principles modeling of SrTiO3 based oxides for thermoelectric applications. J Phys Chem C 2016;120:25678–88. https://doi.org/10.1021/acs.jpcc.6b07634.

[149] Amin B, Eckern U, Schwingenschlögl U. Thermoelectric properties of the misfit cobaltate Ca3Co4O9. Appl Phys Lett 2017;110:233505. https://doi.org/10.1063/1.4984960.

[150] Li W, Carrete J, Katcho NA, Mingo N. ShengBTE: a solver of the Boltzmann transport equation for phonons. Comput Phys Commun 2014;185:1747–58. https://doi.org/10.1016/j.cpc.2014.02.015.

[151] Puligheddu M, Xia Y, Chan M, Galli G. Computational prediction of lattice thermal conductivity: a comparison of molecular dynamics and Boltzmann transport approaches. Phys Rev Mater 2019;3:085401. https://doi.org/10.1103/PhysRevMaterials.3.085401.

[152] Progelhof RC, Throne JL, Ruetsch RR. Methods for predicting the thermal conductivity of composite systems: a review. Polym Eng Sci 1976;16:615–25. https://doi.org/10.1002/pen.760160905.

[153] Landauer R. The electrical resistance of binary metallic mixtures. J Appl Phys 1952;23:779–84. https://doi.org/10.1063/1.1702301.

[154] Sonntag J. Thermoelectric power in alloys with phase separation (composites). J Phys Condens Matter 2009;21. https://doi.org/10.1088/0953-8984/21/17/175703.

[155] Chung DDL. Electrically conductive cement-based materials.pdf. Adv Cement Res 2004;4:167–76. https://doi.org/10.1680/adcr.2004.16.4.167.

[156] Luo Y, Zhang L, Liu Z, Wu J, Zhang Y, Wu Z. Numerical evaluation on energy saving potential of a solar photovoltaic thermoelectric radiant wall system in cooling dominant climates. Energy 2018;142:384–99. https://doi.org/10.1016/j.energy.2017.10.050.

[157] Yazawa K, Shakouri A. Cost-efficiency trade-off and the design of thermoelectric power generators. Environ. Sci. Technol. 2011;45(17):7548–53. https://doi.org/10.1021/es2005418.

[159] Fraisse G, Ramousse J, Sgorlon D, Goupil C. Comparison of different modeling approaches for thermoelectric elements. Energy Convers Manag 2013;65:351–6. https://doi.org/10.1016/j.enconman.2012.08.022.

[160] Koh YR, Yazawa K, Shakouri A. Impact of material properties on cooling COP of integrated thermoelectric microcoolers. ASME 2013 Int. Tech. Conf. Exhib. Packag. Integr. Electron. Photonic Microsystems, InterPACK 2013;2. https://doi.org/10.1115/IPACK2013-73184.

[161] Rowe DM. Thermoelectrics handbook: macro to nano. Thermoelectr Handb Macro to Nano 2005;80:1014. https://doi.org/10.1038/ki.2011.318.

[162] Enescu D. Thermoelectric refrigeration principles. Bringing thermoelectr. Into real. InTech; 2018. https://doi.org/10.5772/intechopen.75439.

[163] Zhang X, Zhao L-DD. Thermoelectric materials: energy conversion between heat and electricity. J Mater 2015;1:92–105. https://doi.org/10.1016/j.jmat.2015.01.001.

[164] Böttner H. Micropelt miniaturized thermoelectric devices: small size, high cooling power densities, short response time. Int. Conf. Thermoelectr. ICT, Proc. 2005; 2005:1–8. https://doi.org/10.1109/ICT.2005.1519873.

[165] Yang J, Caillat T. Thermoelectric materials for space and automotive power generation. MRS Bull 2006;31:224–9. https://doi.org/10.1557/mrs2006.49.

[166] Rehman NU, Siddiqui MA. Performance model and sensitivity analysis for a solar thermoelectric generator. J Electron Mater 2017;46:1794–805. https://doi.org/10.1007/s11664-016-5230-x.

[167] Manikandan S, Kaushik SC. The influence of Thomson effect in the performance optimization of a two stage thermoelectric generator. Energy 2016;100:227–37. https://doi.org/10.1016/j.energy.2016.01.092.

[168] Chen J, Yan Z, Wu L. The influence of Thomson effect on the maximum power output and maximum efficiency of a thermoelectric generator. J Appl Phys 1996; 79:8823–8. https://doi.org/10.1063/1.362507.

[169] Huang MJ, Yen RH, Wang AB. The influence of the Thomson effect on the performance of a thermoelectric cooler. Int J Heat Mass Tran 2005;48:413–8. https://doi.org/10.1016/j.ijheatmasstransfer.2004.05.040.

[170] Xiao H, Gou X, Yang S. Detailed modeling and irreversible transfer process analysis of a multi-element thermoelectric generator system. J Electron Mater 2011;40:1195–201. https://doi.org/10.1007/s11664-011-1596-y.

[171] Rabari R, Mahmud S, Dutta A, Biglarbegian M. Effect of convection heat transfer on performance of waste heat thermoelectric generator. Heat Tran Eng 2015;36: 1458–71. https://doi.org/10.1080/01457632.2015.1010925.

[172] Goupil C. Continuum theory and modeling of thermoelectric elements. n.d.

[173] Shuvalov LA. Transport phenomena in crystals. Mod. Crystallogr. IV. Berlin, Heidelberg: Springer; 1988. p. 376–404. https://doi.org/10.1007/978-3-642-81838-7_6.

[174] Dongxu J, Pou J, Roshan RJ, Romagnoli A. Influence of boundary condition assumption on thermoelectric generator geometry design. Asian conf. Energy, power transp. electrif. ACEPT 2017, 2017– December. Institute of Electrical and Electronics Engineers Inc.; 2017. p. 1–5. https://doi.org/10.1109/ACEPT.2017.8168550.

[175] Alata M, Al-Nimr MA, Naji M. Transient behavior of a thermoelectric device under the hyperbolic heat conduction model. Int J Thermophys 2003;24: 1753–68. https://doi.org/10.1023/B:IJOT.0000004103.26293.0c.

[176] Naji M, Alata M, Al-Nimr MA. Transient behaviour of a thermoelectric device. Proc Inst Mech Eng Part A J Power Energy 2003;217:615–21. https://doi.org/10.1177/095765090321700604.

[177] Castillo EE, Hapenciuc CL, Borca-Tasciuc T. Thermoelectric characterization by transient Harman method under nonideal contact and boundary conditions. Rev Sci Instrum 2010;81. https://doi.org/10.1063/1.3374120.

[178] Moser A, Erd M, Kostic M, Cobry K, Kroener M, Woias P. Thermoelectric energy harvesting from transient ambient temperature gradients. J Electron Mater 2012; 41:1653–61. https://doi.org/10.1007/s11664-011-1894-4.

[179] Kumar S, Heister SD, Xu X, Salvador JR, Meisner GP. Thermoelectric generators for automotive waste heat recovery systems part I: numerical modeling and baseline model analysis. J Electron Mater 2013;42:665–74. https://doi.org/10.1007/s11664-013-2471-9.

[180] Lossec M, Multon B, Ben Ahmed H, Goupil C. Thermoelectric generator placed on the human body: system modeling and energy conversion improvements. EPJ Appl Phys 2010;52. https://doi.org/10.1051/epjap/2010121.

[181] Xiao H, Gou X, Yang C. Simulation analysis on thermoelectric generator system performance. 2008. p. 1183–7. https://doi.org/10.1109/ASC-ICSC.2008.4675546. Asia Simul. Conf. - 7th Int. Conf. Syst. Simul. Sci. Comput. ICSC 2008, 2008,.

[182] Bahk JH, Youngs M, Yazawa K, Shakouri A, Pantchenko O. An online simulator for thermoelectric cooling and power generation. Proc. - Front. Educ. Conf. FIE 2013:1757–9. https://doi.org/10.1109/FIE.2013.6685139.
[183] Lemke N, Koehler J, Junior C, Richter C, Tegethoff W, Köhler J. Modeling and simulation of a thermoelectric heat exchanger using the object-oriented library TIL thermoelectric energy recuperation for aviation (TERA) view project thermodynamik kompakt view project modeling and simulation of a thermoelectric heat exchanger using the object-oriented Library TIL. n.d.
[184] Phillip N, Maganga O, Burnham KJ, Dunn J, Rouaud C, Ellis MA, et al. Modelling and simulation of a thermoelectric generator for waste heat energy recovery in low carbon vehicles. Int. Symp. Environ. Friendly Energies Appl. EFEA 2012; 2012:94–9. https://doi.org/10.1109/EFEA.2012.6294079.
[185] Chakraborty A, Saha BB, Koyama S, Ng KC. Thermodynamic modelling of a solid state thermoelectric cooling device: temperature-entropy analysis. Int J Heat Mass Tran 2006;49:3547–54. https://doi.org/10.1016/j.ijheatmasstransfer.2006.02.047.
[186] Du CY, Wen C Da. Experimental investigation and numerical analysis for one-stage thermoelectric cooler considering Thomson effect. Int J Heat Mass Tran 2011;54:4875–84. https://doi.org/10.1016/j.ijheatmasstransfer.2011.06.043.
[187] Kaushik SC, Manikandan S. The influence of Thomson effect in the energy and exergy efficiency of an annular thermoelectric generator. Energy Convers Manag 2015;103:200–7. https://doi.org/10.1016/j.enconman.2015.06.037.
[188] Wang Y, Zhang M, Tian Y, Wu Z, Xing J, Li Y, et al. Influence of Thomson effect on efficiency of thermoelectric generator. Int Heat Transf Conf 2018;2018-Augus: 6089. https://doi.org/10.1016/j.ijheatmasstransfer.2019.03.155.
[189] Wee D. Analysis of thermoelectric energy conversion efficiency with linear and nonlinear temperature dependence in material properties. Energy Convers Manag 2011;52:3383–90. https://doi.org/10.1016/j.enconman.2011.07.004.
[190] Sherman B, Heikes RR, Ure RW. Calculation of efficiency of thermoelectric devices. J Appl Phys 1960;31:1–16. https://doi.org/10.1063/1.1735380.
[191] Drabkin IA, Ershova LB. Comparison of approaches to thermoelectric modules mathematical optimization. Int. Conf. Thermoelectr. ICT, Proc. 2006:476–9. https://doi.org/10.1109/ICT.2006.331319.
[192] Parrott JE. The interpretation of the stationary and transient behaviour of refrigerating thermocouples. Solid State Electron 1960;1:135–43. https://doi.org/10.1016/0038-1101(60)90045-9.
[193] Huang BJ, Duang CL. System dynamic model and temperature control of a thermoelectric cooler. Int J Refrig 2000;23:197–207. https://doi.org/10.1016/S0140-7007(99)00045-6.
[194] Tsai HL, Lin JM. Model building and simulation of thermoelectric module using Matlab/Simulink. J Electron Mater 2010;39:2105–11. https://doi.org/10.1007/s11664-009-0994-x.
[195] Crane DT. An introduction to system-level, steady-state and transient modeling and optimization of high-power-density thermoelectric generator devices made of segmented thermoelectric elements. J Electron Mater 2011;40:561–9. https://doi.org/10.1007/s11664-010-1451-6.
[196] Md Yusop A, Mohamed R, Ayob A. Model building of thermoelectric generator exposed to dynamic transient sources. IOP Conf Ser Mater Sci Eng 2013;53. https://doi.org/10.1088/1757-899X/53/1/012015.
[197] Lineykin S, Ben-Yaakov S. Modeling and analysis of thermoelectric modules. IEEE Trans Ind Appl 2007;43:505–12. https://doi.org/10.1109/TIA.2006.889813.
[198] Chen M, Gao J, Kang Z, Zhang J. Design methodology of large-scale thermoelectric generation: a hierarchical modeling approach. J Therm Sci Eng Appl 2012;4. https://doi.org/10.1115/1.4007223.
[199] Chen M, Bach IP, Rosendahl L, Condra T, Pedersen JK. Notes on computational methodology and tools of thermoelectric energy systems. 2007.
[200] Chávez JA, Ortega JA, Salazar J, Turó A, García MJ, Catalunya UP, et al. SPICE model of thermoelectric elements including thermal effects. 2000. https://doi.org/10.1109/IMTC.2000.848895.
[201] Lineykin S, Ben-Yaakov S. Analysis of thermoelectric coolers by a spice-compatible equivalent-circuit model. IEEE Power Electron Lett 2005;3:63–6. https://doi.org/10.1109/LPEL.2005.846822.
[202] Mitrani D, Tome JA, Salazar J, Turo A, Garcia MJ, Chavez JA. Methodology for extracting thermoelectric module parameters. IEEE Trans Instrum Meas 2005;54: 1548–52. https://doi.org/10.1109/TIM.2005.851473.
[203] Hogan TP. Modeling and characterization of power generation modules based on bulk materials. 2006.
[204] Fateh H, Baker CA, Hall MJ, Shi L. High fidelity finite difference model for exploring multi-parameter thermoelectric generator design space. Appl Energy 2014;129:373–83. https://doi.org/10.1016/j.apenergy.2014.04.088.
[205] Dgheim J, Chahine A, Ghazeleh M, Abdallah M. Numerical computation OF thermoelectric efficiency OF graphite sheet optimal dimension. Leban Sci J 2019; 20. https://doi.org/10.22453/LSJ-020.1.122-133.
[206] Yan D, Dawson FP, Pugh MC, El-Deib A. Time dependent finite volume model of thermoelectric devices. IEEE Energy Convers. Congr. Expo., IEEE; 2012. p. 105–12. https://doi.org/10.1109/ECCE.2012.6342835.
[207] Oliveira KSM, Cardoso RP, Hermes CJL. Two-dimensional modeling of thermoelectric cells. n.d.
[208] Oliveira KSM, Cardoso RP, Hermes CJL. Numerical assessment of the thermodynamic performance of thermoelectric cells via two-dimensional modelling. Appl Energy 2014;130:280–8. https://doi.org/10.1016/j.apenergy.2014.05.050.
[209] Pfeiffelmann B, Benim AC, Joos F. A finite volume Analysis of thermoelectric generators. Heat Tran Eng 2018;7632:1–9. https://doi.org/10.1080/01457632.2018.1474588.
[210] Chen M, Rosendahl LA, Condra T. A three-dimensional numerical model of thermoelectric generators in fluid power systems. Int J Heat Mass Tran 2011;54: 345–55. https://doi.org/10.1016/j.ijheatmasstransfer.2010.08.024.
[211] Antonova EE, Looman DC. Finite elements for thermoelectric device analysis in ANSYS. ICT; 2005. p. 215–8. https://doi.org/10.1109/ICT.2005.1519922. 24th Int. Conf. Thermoelectr. 2005., IEEE; 2005, p.
[212] Saber HH, El-Genk MS. A three-dimensional, performance model of segmented thermoelectric converters. AIP Publishing; 2007. p. 998–1006. https://doi.org/10.1063/1.1449830.
[213] Jaegle M. Multiphysics simulation of thermoelectric systems-modeling of peltier-cooling and thermoelectric generation. n.d.
[214] Topal ET. A flow induced vertical thermoelectric generator and its simulation using COMSOL Multiphysics. n.d.
[215] Martin J. Computational Seebeck coefficient measurement simulations. J Res Natl Inst Stand Technol 2012;168. https://doi.org/10.6028/jres.117.009.
[216] Ebling D, Jaegle M, Bartel M, Jacquot A, Böttner H. Multiphysics simulation of thermoelectric systems for comparison with experimental device performance. J Electron Mater 2009;38:1456–61. https://doi.org/10.1007/s11664-009-0825-0.
[217] Bermúdez A, Gómez D, Muñiz MC, Salgado P. Transient numerical simulation of a thermoelectrical problem in cylindrical induction heating furnaces. Adv Comput Math 2007;26:39–62. https://doi.org/10.1007/s10444-005-7470-9.
[218] Bitschi A. Modelling of thermoelectric devices for electric power generation. 2009. https://doi.org/10.3929/ETHZ-A-005936533.
[219] Hu X, Takazawa H, Nagase K, Ohta M, Yamamoto A. Three-dimensional finite-element simulation for a thermoelectric generator module. J Electron Mater 2015; 44:3637–45. https://doi.org/10.1007/s11664-015-3898-y.
[220] Wu G, Yu X. A comprehensive 3D finite element model of a thermoelectric module used in a power generator: a transient performance perspective. J Electron Mater 2015;44:2080–8. https://doi.org/10.1007/s11664-015-3664-1.
[221] Al-Merbati AS, Yilbas BS, Sahin AZ. A model study for cyclic thermal loading and thermal performance of a thermoelectric generator. Int J Energy Res 2014;38: 1351–60. https://doi.org/10.1002/er.3152.
[222] Bals A, Barnes N, Bravo R, Garcia N. Biosensor using P. Powering a biosensor using wearable thermoelectric technology. 2018.
[223] Zhang J, Zavaliangos A. Discrete finite-element simulation of thermoelectric phenomena in spark plasma sintering. J Electron Mater 2011;40:873–8. https://doi.org/10.1007/s11664-011-1606-0.
[224] Gigliotti M, Marchand D, Lafarie-Frenot MC, Grandidier JC. Thermoelectric behaviour OF composite materials for aircraft applications. n.d.
[225] Ting H. Thermoelectric coupling simulation lightning damage of aircraft composite. SAVE Proc 2016:35–40. https://doi.org/10.1109/ICMAE.2016.7549504. 2016 7th Int. Conf. Mech. Aerosp. Eng. ICMAE 2016, Institute of Electrical and Electronics Engineers Inc.
[226] Mani PI. ScholarWorks at WMU design, modeling and simulation of a thermoelectric cooling system (TEC). n.d.
[227] Assefa M, Lai X, Liu L, Liao Y. Peridynamic formulation for coupled thermoelectric phenomena. Ann Mater Sci Eng 2017;2017. https://doi.org/10.1155/2017/9836741.
[228] Theses G, McKnight PT, Patrick McKnight by T, Professor M, Crane N, Pyrtle F, et al. Scholar commons finite element analysis of thermoelectric systems with applications in self assembly and haptics scholar commons citation finite element analysis of thermoelectric systems with applications in self assembly and haptics. n.d.
[229] Richter CC, Braunschweig : proposal of new object-oriented equation-based model libraries for thermodynamic systems. n.d.
[230] Felgner F, Frey G. Object-oriented simulation model of thermoelectric devices for energy system design. Proc Mediterr Electrotech Conf - MELECON 2012:577–80. https://doi.org/10.1109/MELCON.2012.6196499.
[231] Felgner F, Exel L, Nesarajah M, Frey G. Component-oriented modeling of thermoelectric devices for energy system design. IEEE Trans Ind Electron 2014; 61:1301–10. https://doi.org/10.1109/TIE.2013.2261037.
[232] Nesarajah M, Exel L, Frey G. Modelica® library for dynamic simulation of thermoelectric generators. Proc. 11th eur. Conf. Thermoelectr. Springer International Publishing; 2014. p. 213–7. https://doi.org/10.1007/978-3-319-07332-3_25.
[233] Nesarajah M, Frey G. Thermoelectric applications for home use: thermostat and green barbecue 2.0. Mater. Today Procvol. 5. Elsevier Ltd; 2018. p. 10283–90. https://doi.org/10.1016/j.matpr.2017.12.275.
[234] Nesarajah M, Frey G. Optimized design of thermoelectric energy harvesting systems for waste heat recovery from exhaust pipes. Appl Sci 2017;7. https://doi.org/10.3390/app7060634.
[235] Nesarajah M, Felgner F, Frey G. Model-based system Assessment OF thermoelectric energy harvesting from the exhaust gas pipe OF oil-fired heatings. MM Sci J 2015;2015:570–5. https://doi.org/10.17973/MMSJ.2015_03_201507.
[236] Whittles TJ. Introduction. Cham: Springer; 2018. https://doi.org/10.1007/978-3-319-91665-1_1.
[237] Datta S. Lessons from nanoelectronics. World Scientific; 2018. https://doi.org/10.1142/10440-vol2.
[238] Hong M, Chen ZG, Zou J. Fundamental and progress of Bi2Te3-based thermoelectric materials. Chin Phys B 2018;27. https://doi.org/10.1088/1674-1056/27/4/048403.
[239] Thomson William. On a mechanical theory of thermo-electric currents. Proc R Soc Edinburgh Sect A Math Phys Sci 1963;66:f1–2. https://doi.org/10.1017/s0080454100007767.
[240] Pop E, Edu S. Thermoelectrics 101. n.d.

[241] Goldsmid HJ. Introduction to thermoelectricity. Springer Series in Materials Science); 2009. https://doi.org/10.1007/978-3-642-00716-3.
[242] Mahan G, Sales B, Sharp J. Thermoelectric materials: new approaches to an old problem. Phys Today 1997;50:42–7. https://doi.org/10.1063/1.881752.
[243] Chaikin PM. An introduction to thermopower for those who might want to use it to study organic conductors and superconductors. Org. Supercond. Springer US; 1990. p. 101. https://doi.org/10.1007/978-1-4899-2605-0_11.
[244] Tritt TM. Thermoelectric phenomena, materials, and applications. Annu Rev Mater Res 2011;41:433–48. https://doi.org/10.1146/annurev-matsci-062910-100453.
[245] F Mott N, Davis EA. Electronic processes in the non crystalline materials. New York: Oxford University Press Inc.; 2012.
[246] Sootsman JR, Chung DY, Kanatzidis MG. New and old concepts in thermoelectric materials. Angew Chem Int Ed 2009;48:8616–39. https://doi.org/10.1002/anie.200900598.
[247] Tritt TM, Subramanian MA. Thermoelectric materials, phenomena, and applications: a bird's eye view. MRS Bull 2006;31:188–98. https://doi.org/10.1557/mrs2006.44.
[248] Tritt TM. Recent trends in thermoelectric materials research II. Academic Press; 2001.
[249] DiSalvo FJ. Thermoelectric cooling and power generation. Science 1999;285:703–6. https://doi.org/10.1126/SCIENCE.285.5428.703.
[250] Heremans JP, Jovovic V, Toberer ES, Saramat A, Kurosaki K, Charoenphakdee A, et al. Enhancement of thermoelectric efficiency in PbTe by distortion of the electronic density of states. Science 2008;321:554–7. https://doi.org/10.1126/SCIENCE.1159725.
[251] Hicks LD, Dresselhaus MS. Thermoelectric figure of merit of a one-dimensional conductor. Phys Rev B 1993;47:16631–4. https://doi.org/10.1103/PhysRevB.47.16631.
[252] Hicks LD, Dresselhaus MS. Effect of quantum-well structures on the thermoelectric figure of merit. Phys Rev B 1993;47:12727–31. https://doi.org/10.1103/PhysRevB.47.12727.
[253] Nozariasbmarz A, Agarwal A, Coutant ZA, Hall MJ, Liu J, Liu R, et al. Thermoelectric silicides: a review. Jpn J Appl Phys 2017;56:05DA04. https://doi.org/10.7567/JJAP.56.05DA04.
[254] Pei Y, Wang H, Snyder GJ. Band engineering of thermoelectric materials. Adv Mater 2012;24:6125–35. https://doi.org/10.1002/adma.201202919.
[255] Biswas K, He J, Blum ID, Wu C-I, Hogan TP, Seidman DN, et al. High-performance bulk thermoelectrics with all-scale hierarchical architectures. Nature 2012;489:414–8. https://doi.org/10.1038/nature11439.
[256] Ravich YI, Efimova BA, Tamarchenko VI. Scattering of current carriers and transport phenomena in lead chalcogenides. Phys Status Solidi 1971;43:11–33. https://doi.org/10.1002/pssb.2220430102.
[257] Spaepen F. Solid state physics : advances in research and applications, ume 51. Academic Press; 1998.
[258] Zheng J. Recent advances on thermoelectric materials. Front Phys China 2008;3:269–79. https://doi.org/10.1007/s11467-008-0028-9.
[259] Zhang J, Liu R, Cheng N, Zhang Y, Yang J, Uher C, et al. High-performance pseudocubic thermoelectric materials from non-cubic chalcopyrite compounds. Adv Mater 2014;26:3848–53. https://doi.org/10.1002/adma.201400058.
[260] Slack GA. Design concepts for improved thermoelectric materials. Mater Res Soc Symp - Proc 1997;478:47–54. https://doi.org/10.1557/proc-478-47.
[261] Slack G. New materials and performance limits for thermoelectric cooling. CRC Handb. Thermoelectr., CRC Press; 1995. p. 407–40. https://doi.org/10.1201/9781420049718.ch34.
[262] Fu C, Wu H, Liu Y, He J, Zhao X, Zhu T. Enhancing the figure of merit of heavy-band thermoelectric materials through hierarchical phonon scattering. Adv Sci 2016;3:1600035. https://doi.org/10.1002/advs.201600035.
[263] Liu W, Yan X, Chen G, Ren Z. Recent advances in thermoelectric nanocomposites. Nanomater Energy 2012;1:42–56. https://doi.org/10.1016/j.nanoen.2011.10.001.
[264] Minnich AJ, Dresselhaus MS, Ren ZF, Chen G. Bulk nanostructured thermoelectric materials: current research and future prospects. Energy Environ Sci 2009;2:466. https://doi.org/10.1039/b822664b.
[265] Dresselhaus MS, Chen G, Tang MY, Yang RG, Lee H, Wang DZ, et al. New directions for low-dimensional thermoelectric materials. Adv Mater 2007;19:1043–53. https://doi.org/10.1002/adma.200600527.
[266] Troncoso JF, Aguado-Puente P, Kohanoff J. Effect of intrinsic defects on the thermal conductivity of PbTe from classical molecular dynamics simulations. 2018.